Carrier Lifetime and Diffusion Measurement using Free-carrier Absorption Imaging

Carrier Lifetime and Diffusion Measurement using Free-carrier Absorption Imaging

By

Shuaiwen Gao

B.Eng.

A Thesis

Submitted to the School of Graduate Studies

in Partial Fulfillment of the Requirements

for the Degree

Master of Applied Science

McMaster University

MASTER OF APPLIED SCIENCE (2020) MCMASTER UNIVERSITY

Department of Engineering Physics Hamilton, Ontario

TITLE: Carrier Lifetime and Diffusion Measurement using Free-carrier Absorption Imaging

AUTHOR: SHUAIWEN GAO, B.Eng., (Nanjing University of Science and Technology, Nanjing, China)

SUPERVISOR: Professor Rafael N. Kleiman

NUMBER OF PAGES: IX, 73

Abstract

At the moment, when energy and environmental issues are of concerned in our society, photovoltaic technology has received tremendous development and demand. Because carrier lifetime and diffusion coefficient are the important indicators to determine the recombination level, which influences the efficiency of solar cells to a large extent, they are regarded as key in choosing solar cell materials. A technique for effective lifetime measurement, modulated free-carrier absorption (FCA), can extract lifetime and diffusion coefficient simultaneously, which is supported by a general mathematical model that predicts the experimental signal accounting for the 3-dimensional (3D) charge-carrier transport and recombination within the semiconductor. A single mode 1064 nm laser modulated by an EO modulator is used as the pump and a 2050 nm modulated LED is used as probe in this experiment as the pump/probe parts. An IR camera detects the frequency-domain diffusion image from the tested silicon sample at the tested frequency range between 1 kHz to 200 kHz and the lifetime can be extracted by frequency-domain free-carrier concentration equation, which is a Lorentzian model. By simulating the diffusion data from the camera with the 3D free-carrier absorption model, we can extract lifetime and diffusion coefficient simultaneously. The fitted lifetime from frequency-domain free-carrier absorption equation is 33.5 ± 1.3 μs, and the fitted lifetime from this 3D FCA model is 32.8 ± 1.5 μs, which match to within the error bars. The fitted diffusion coefficient from this 3D FCA model is 15.6 ± 0.7 cm^2/s, which agrees with the theoretical value of 16 cm^2/s for silicon. Good quantitative agreement is found among the model, experimental data, and theory.

Acknowledgements

I’m grateful to have the chance to study in McMaster as a Master of Science. From this period, I learned a lot knowledge and built my basic scientific literacy with the help of all the kind and knowledgeable people on and off campus. I would like to express my sincere gratitude for my supervisor, Prof. Rafael N. Kleiman, who always gives me constant support, guidance and encouragement since I joined his research group. He is so understandable, considerate and patient that can guide me to the proper path when I face academic difficulties and support me to try different things besides research for comprehensive development. I do feel honored to have the opportunity to join his research group and learn from him.

I would like to thank Dr. Kevin M.W. Boyd, who has helped me a lot in this work. He unselfishly shared his knowledge, helped and taught me to solve the difficulties encountered in the experiment, and helped me quickly understand the principle when I started doing this experiment. I am honored to have colleagues like him. Besides of Dr. Boyd, I also would like to thank my colleague Ruslan Khabibrakhmanov, David McShannon and Taz Colangelo who always brings up fantastic ideas in the weekly group meeting that give me great inspiration. I also want to thank Elias Vitali and Yinfei Li who have contributed in this experiment.

I would like to thank Dr. Peter Mascher, Dr. Chang-qing Xu, Dr. Andy Knights and Dr. Adrian Kitai, who have instructed academic courses I’ve attended. They are knowledgeable, thoughtful enough to make their courses well-organized, helpful and thought-provoking, from which I learnt the knowledge of my field and built the foundation of my thesis.

I would like to thank Dr. Jonathan Bradley, Dr. Adriaan Buijs who chose me as their TA, as well

as Peter Jonasson, the lab technician who guided me to help students with their experiments for Dr. Bradley’s course. They are reliable, considerable and professional to help me finish the TA duties, from which I gained a lot experience on teaching students and communicating with others.

I would like to thank the department administrator, Robert Laidler, the graduate administrative assistant, Nicole Macdonald and former graduate administrative assistant, Marilyn Marlow, who did great administrative work and made me feel comfortable to concentrate on my research.

Last but not least, I want to express my heartfelt gratitude for my parents for their constant support, encouragement and understanding through the entire journey of my graduate life.

Table of Contents

List of Figures

List of Tables

1. Introduction:

1.1. Background of Photovoltaics

Photovoltaics (PV) is the conversion of light into electricity using semiconducting materials that exhibit the photovoltaic effect, a phenomenon studied in physics, photochemistry, and electrochemistry. Photovoltaic technology has many advantages. It does not have any mechanical moving parts; it does not need any "fuel" except for sunlight; it can work under direct sunlight and oblique radiation; it is very convenient and flexible from the choice of site, which can be applied on roofs and open spaces in the city. Since 1958, the solar photovoltaic effect has been applied for the first time in the form of solar cells in the energy supply of space satellites. Today, from the power supply of the automatic parking meter, the rooftop solar panel, to the large-scale solar power generation center, its application in the field of power generation has spread all over the world. Solar photovoltaics is growing rapidly. Figure 1.1 shows the growth of photovoltaics since 2009.

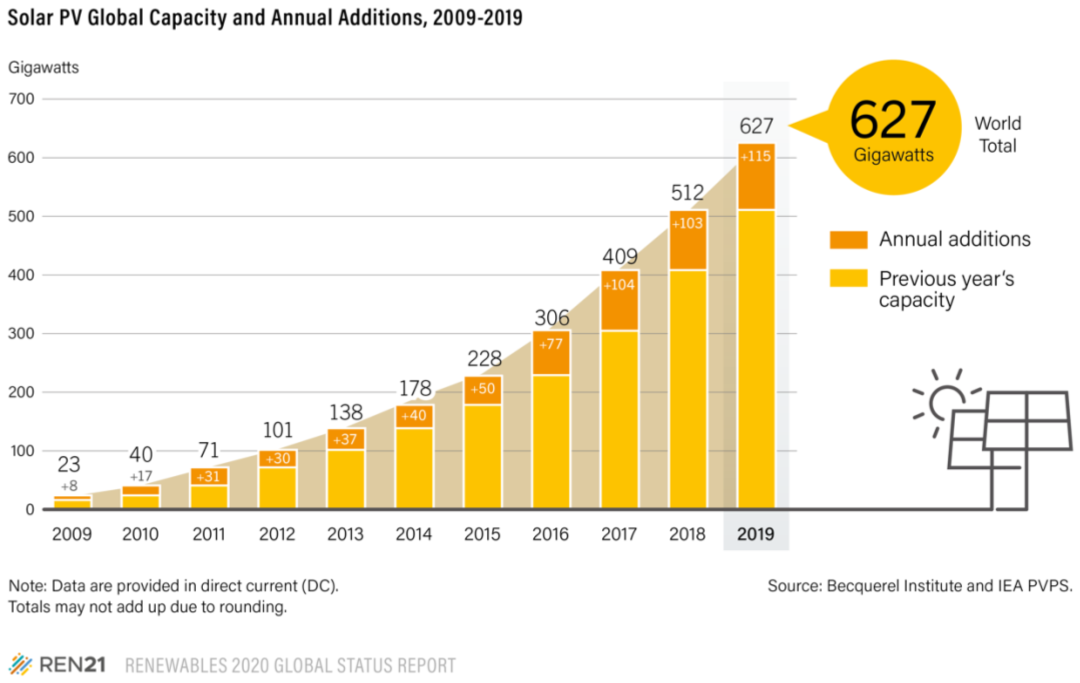
Solar PV Global Capacity and Annual Additions, 2009-2019

Note: Data are provided in direct current (DC).
Totals may not add up due to rounding.

Source: Becquerel Institute and IEA PVPS.

REN21 RENEWABLES 2020 GLOBAL STATUS REPORT

Figure 1.1 Exponential Growth of Solar PV [1].

The total world PV capacity is now beyond 600 TWh of electricity. This represents 2% of worldwide electricity demand. More than 100 countries use solar PV [2] and among them, at least 39 countries had a cumulative solar PV capacity of 1 GW or more [1].

Solar cells are used to convert energy from the sun into a flow of electrons by the photovoltaic effect in photovoltaics industry [3,4]. The principle of a solar cell is as follows: a diode composed of a semiconductor material absorbs the energy of photons in sunlight, and transmits energy to electrons, which are driven by a built-in electric field in the diode to generate a photocurrent. Photons have energy, and each semiconductor material has a property--bandgap. If the photon energy is larger than this bandgap, the photons can be absorbed. The photon absorption coefficient of the semiconductor material determines the light absorption efficiency of the solar cell, which in turn determines the material thickness required to manufacture the solar cell. Figure 1.2 shows this process.

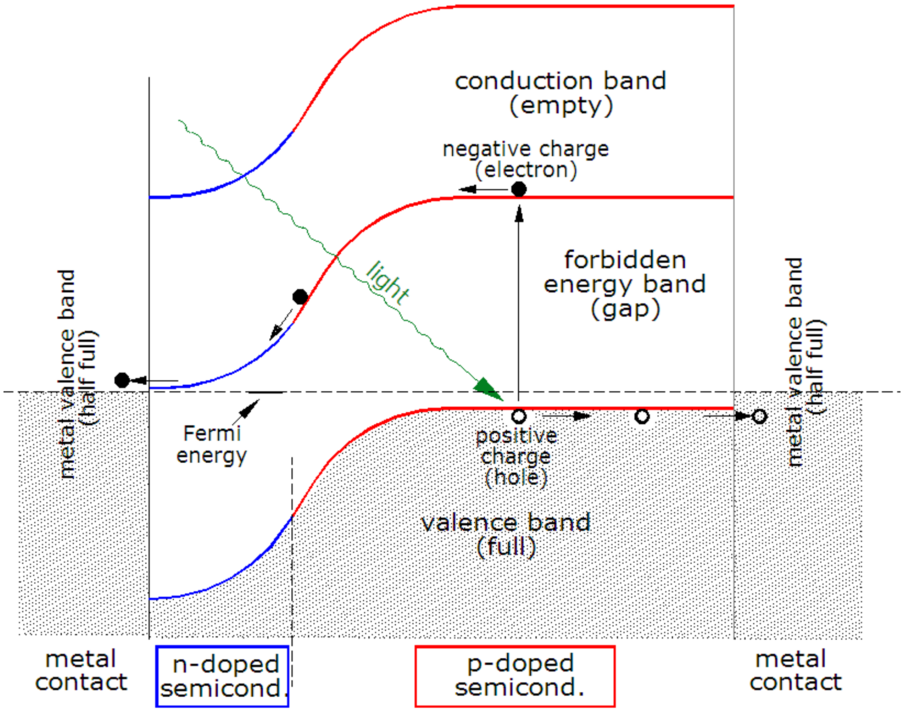

Figure 1.2. Band diagram of a silicon solar cell, corresponding to very low current (horizontal Fermi level), very low voltage (metal valence bands at same height), and therefore very low illumination [5].

Nowadays, research on solar cells is mostly focused on improving the efficiency. Based on the Shockley-Queisser limit, the theoretical maximum efficiency of a single junction solar cell is 33.7% with band gap at 1.34 eV [6]. Figure 1.3 shows this plot. In the extreme, with an infinite number of layers, the corresponding limit is 86% using concentrated sunlight [7].

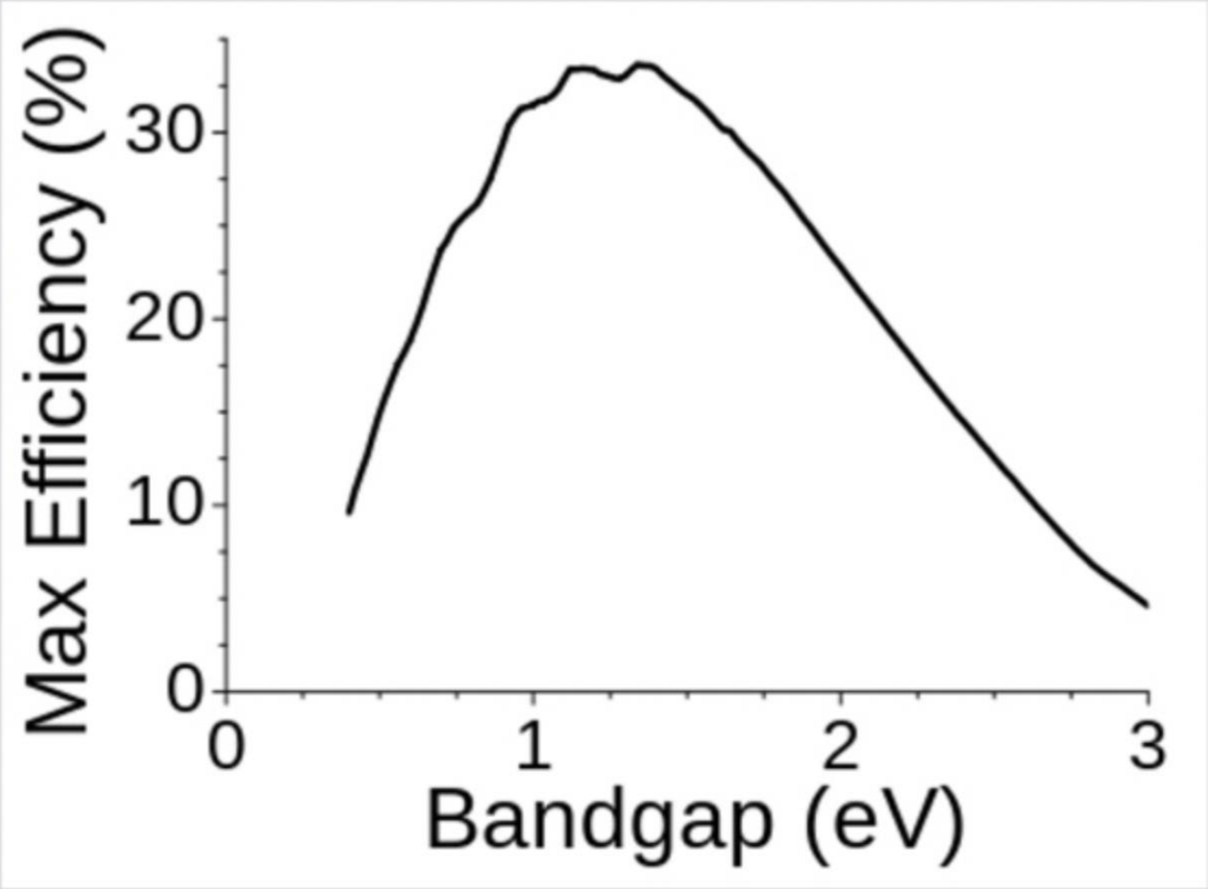

Figure 1.3. Shockley-Queisser limit [8].

The three most important factors that influence the efficiency of the solar cell are absorption coefficient, band gap and recombination rate. Absorption coefficient, which can influence the generation process, determines how far into a material light of a particular wavelength can penetrate before it is absorbed, thus solar cells made by materials with high absorption coefficient can have high efficiency at the same wafer thickness or can be made thinner to match the same efficiency standard. Figure 1.4 shows the absorption coefficient of different materials of the vacuum wavelength of light at 300K.

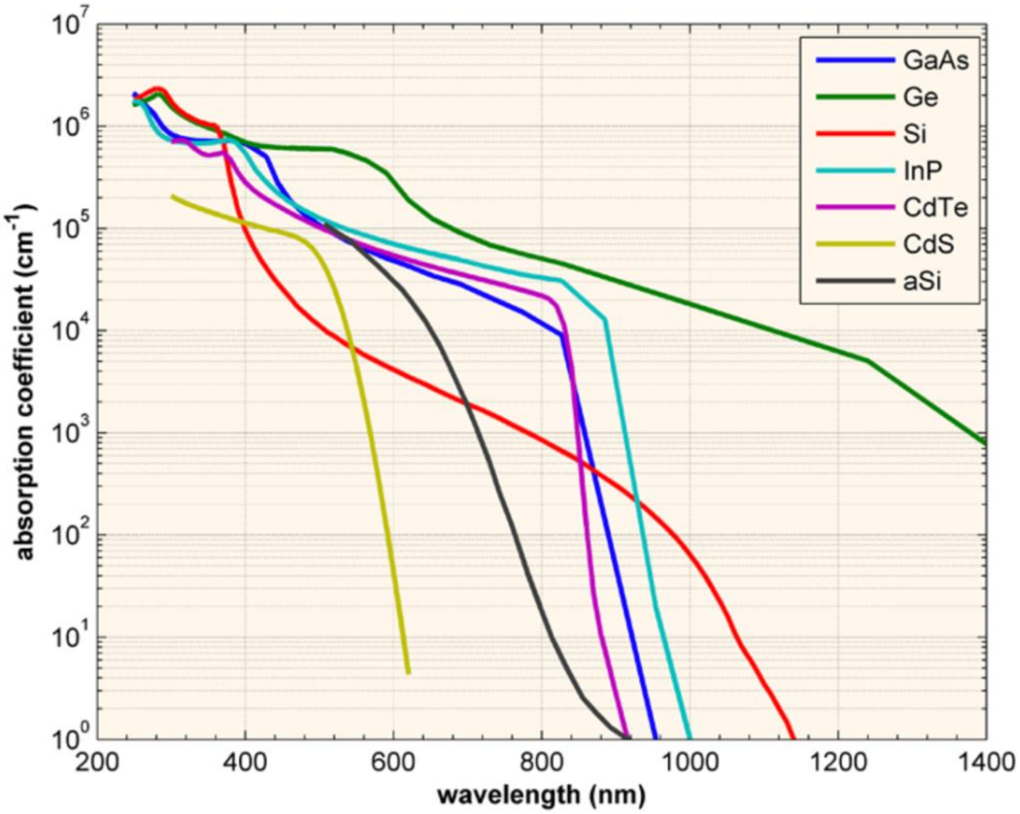

Figure 1.4. The absorption coefficient, α, in a variety of semiconductor materials at 300K as a function of the vacuum wavelength of light [9].

Bandgap, as discussed before, can influence the wavelength range of light to be absorbed by the cell, which can be computed by:

$$\lambda = \frac{1.24}{E_g} \tag{1.1.1}$$

where E_g is the bandgap of the material in eV and λ is the cutoff wavelength in μm. The solar spectrum can be divided into three bands: Ultra-violet light (290-380nm), Visible light (380-780nm) and Infra-red light (780-2500nm). The energy distribution within the solar spectrum is approximately 2% UV, 47% visible and 51% IR. As shown in Figure 1.5, the solar spectrum, most of the IR energy is in the 780-1250 nm range. Taking the Shockley-Queisser limit into account, most of the materials used in single junction solar cells have bandgap between 1-1.5 eV.

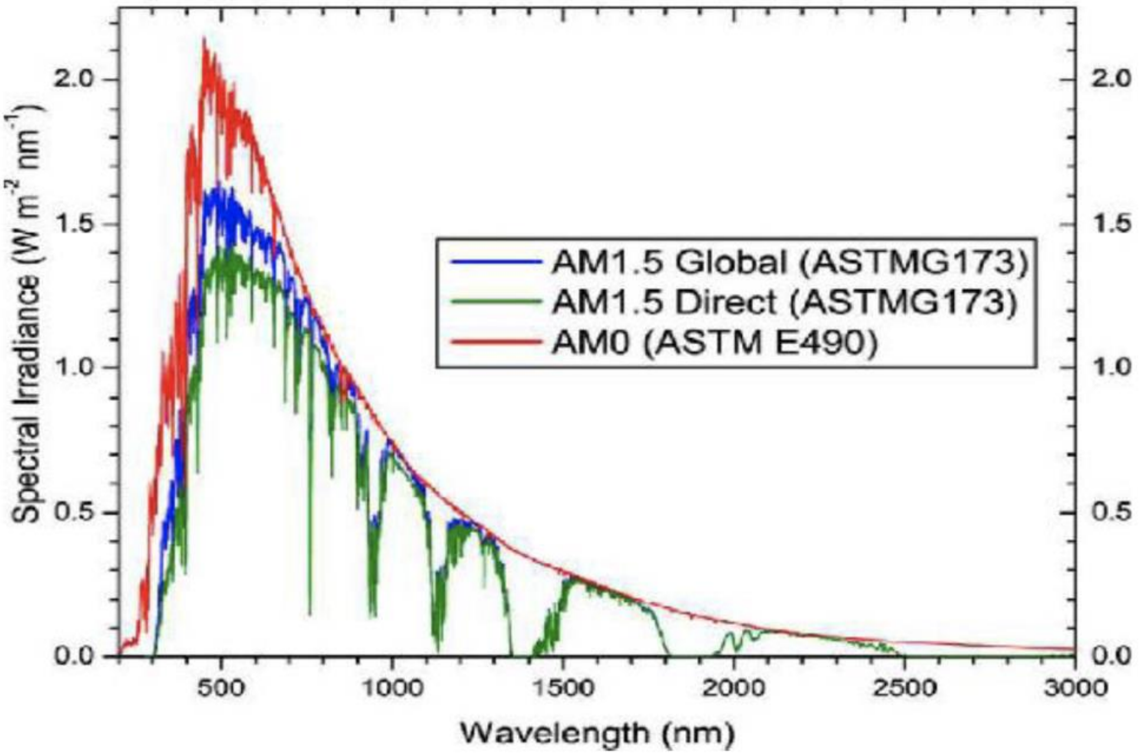

Figure 1.5. Solar Spectrum [10].

Recombination can also influence the efficiency of solar cells, which means generated electrons and holes recombine before going to the cell contacts to generate current. There are several different types of recombination and they are discussed in chapter 2. Instead of measuring recombination rate, we regard lifetime and diffusion coefficient which can be measured or computed from experimental data to be more convenient as the important indicators to present the recombination level and they are key in choosing solar cell materials.

The lifetime of the material takes into account the different types of recombination and can be given by:

$$\tau = \frac{n}{R} \tag{1.1.2}$$

where τ is the minority carrier lifetime, n is the excess minority carrier concentration and R is the recombination rate.

Diffusion coefficient D, as well as lifetime τ, defines diffusion length:

$$L = \sqrt{D\tau} \tag{1.1.3}$$

Diffusion length is the average length a carrier moves between generation and recombination. Higher diffusion lengths are indicative of materials with longer lifetimes. Therefore, methods to measure τ and D are important to PV industry.

1.2. Lifetime Measurement Review

Minority carrier lifetime is an important parameter of semiconductor materials. It has been studied since the beginning of semiconductor development. As early as the 1950s, Shockley and Hall and others had already reported on the theory of minority carrier recombination [11-14]. Afterwards, although some people have studied the lifetime of minority carriers in semiconductors, because of the mismatch between test equipment and measurement standard at that time, it is difficult to prepare samples, especially for the systematic analysis of test results. Therefore, the study of minority carrier lifetime has not attracted widespread attention. It was not until the commercial demand increased that the test of minority carrier lifetime regained people's attention. Crystal manufacturers and IC integrated circuit companies have adopted carrier life testing to monitor the production process. These companies also use carrier lifetime to characterize the cleanliness of the process and they use lifetime to study the causes of device performance degradation. At this time, the corresponding test equipment is required to be non-destructive, non-contact, and non-polluting, and sample preparation cannot be very complicated, thereby promoting the development of test equipment.

However, it is the discovery of the formation and decomposition of iron and boron that plays an important role in the carrier lifetime test [15,16]. At first, this was only regarded as an interesting phenomenon, and it had not been applied to semiconductor testing. Until Zoth and Bergholz discovered that in B-doped semiconductors, by measuring the minority lifetime before and after decomposition of iron and boron, we can obtain the concentration of iron in the sample [17]. In the current crystal growth process, iron, as a constituent element of stainless steel, is an important metal contamination, which is very harmful to microelectronic devices and solar cells. Through the minority carrier lifetime test, the concentration of iron contamination in the semiconductor can be obtained, which is undoubtedly a perfect combination of semiconductor material parameter testing and device performance characterization. After that, the carrier life testing equipment developed rapidly.

At present, the minority carrier lifetime as an important parameter of semiconductor materials has been used as an important reference basis for characterizing device performance and solar cell efficiency. However, due to differences in light injection amount, test frequency, temperature and other parameters of different test equipment, the test values often differ greatly, and the error range may be 100% or more, so there is still something remaining to be improved in lifetime measurement field.

Usually the minority carrier lifetime is measured by experimental methods, and various measurement methods include two basic aspects of non-equilibrium carrier injection and detection. The most commonly used injection methods are light injection and electrical injection, and there are many methods for detecting non-equilibrium carriers, such as detecting changes in electrical conductivity, detecting changes in microwave reflection or transmission signals, etc. This combination forms many lifetime test methods. In the past 30 years, dozens of methods for measuring life have been developed, as shown in Table 1.1.

Minority injection Method	Measuring Method	Measured Value	Measured Range
Photon Injection	Photo Conductivity Decay (PCD)	τ	$\tau > 10^{-7}$s
	Surface photovoltage (SPV)	$L(\tau_b)$	$1 < L < 500\mu m$
	Microwave photoconductivity decay (μ-PCD)	τ	$\tau > 10^{-7}$s
	Quasi-steady state photoconductance (QSSPC)	τ	$\tau > 10^{-7}$s
	Free-Carrier Absorption (FCA)	τ	$\tau > 10^{-5}$s
Electron beam	Scanning Electron Microscopy (SEM)	τ	$\tau > 10^{-9}$s
PN Junction	Diode reverse recovery	τ	$\tau > 10^{-9}$s
MOS device	Step voltage response of MOS capacitor	τ	$\tau_b > 10^{-11}$s
	MOS channel current	τ_b	10^{-14}s $< \tau < 10^{-3}$s

Table 1.1. Minority carrier lifetime test method.

where τ_b is bulk lifetime, which will be discussed in chapter 2.

The three most important techniques for lifetime measurement in silicon are quasi-steady state photoconductance (QSSPC), microwave photoconductance decay (μ-PCD) and pump/probe infrared free-carrier absorption [18]. The main difference between the techniques is the physical quantity used to sense the free-carrier density of an optically excited silicon wafer. The former two methods use RF and microwave-frequency measurements of photoconductivity, while the latter uses the FCA of an infrared probe beam. Figure 1.6 shows a plot of the total number of articles published by year related to the three lifetime metrologies including papers developing the theory and implementation of the techniques, as well as papers applying the techniques to scientific studies.

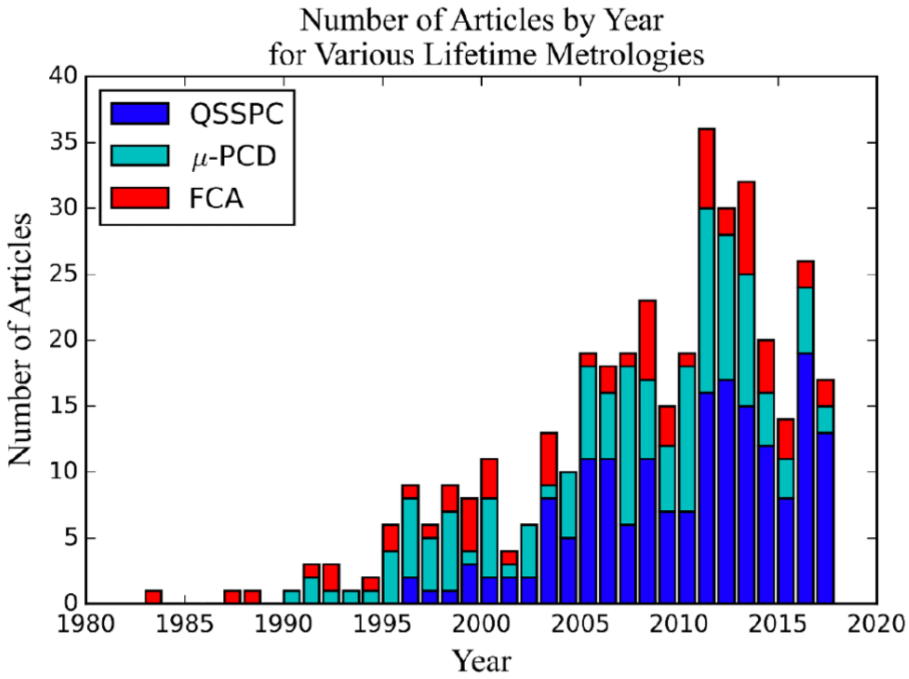

Figure 1.6. Number of Articles per Year for Various Lifetime Metrologies. Three common techniques for lifetime measurements are considered in this plot: QSSPC, μ-PCD, and FCA. Data is obtained from Web of Science analytics [34].

The microwave photoconductivity decay method (μ-PCD) measures the lifetime of minority carriers, which mainly includes the two processes: laser injection generating electron-hole pairs and changes in microwave detection signals. Laser injection generates electron-hole pairs, which leads to an increase in sample conductivity. When external light injection is removed, the conductivity decays exponentially with time. This trend indirectly reflects the decay trend of minority carriers. The changing trend can get the lifetime of minority carriers. This principle is similar to that of DC, or high-frequency photoconductivity. The use of microwave signals to detect changes in conductivity is based on the principle that changes in microwave signals are proportional to changes in conductivity.

The first to propose the use of microwave signals to detect the lifetime of minority carriers in semiconductors was AP Ramsad et al [19]. They used probe electrical injection or optical injection to generate non-equilibrium carriers in germanium. Decay reflects the tendency of minority carriers to recombine, thereby obtaining the lifetime of minority carriers. Compared with the traditional DC photoconductor attenuation method, the minority carrier lifetime value obtained by microwave detection can not only ensure that the deviation is very small, but also avoid the problem of difficult preparation of ohmic electrodes, especially for those semiconductor materials whose performance is not well understood. Because in the traditional DC photoconductor attenuation method, the preparation of ohmic electrodes is a big problem. Therefore, they believe that using microwave methods to detect the minority carrier lifetime in semiconductors has a great advantage over traditional methods. However, H.A. Atwater [20] later deduced through theory that this method has great limitations. He believes that to make the microwave attenuation signal proportional to the carrier attenuation signal, the following conditions must be met. Firstly, the sample must be thin enough, which will lead to increased surface recombination effects and the tested lifetime will deviate from the real lifetime; secondly, it must be ensured that the experiment is under low level injection, which can ensure that the lifetime of minority carriers can decay exponentially, based on the theory of Shockley and others [11, 13, 21]. Because of this problem, there were not as many researches as expected in a long time. After that, Kramer and others [22] used microwave detection methods to study excess carriers in ZnS, CdS and other phosphor powders. In the 1970s, people really started to use microwaves to detect the minority carriers in semiconductors. In the late 1980s, Warman and his collaborators [23,24] used microwave signals to detect the attenuation of carriers in semiconductors, but they were limited to low-conductivity systems. Since then, M. Kunst et al. have extended the scope of application based on Warman's research principles so that it can be applied to semiconductor materials of arbitrary conductivity [25].

Another prominent lifetime measurement tool based on the principle of photoconductivity is *Quasi-Steady State Photoconductance* (QSSPC) [26]. As the name suggests, this approach is a quasi-steady state technique and it extracts lifetime by measuring the absolute amplitude of photoconductivity in quasi-steady state, which is directly related to the free-carrier density via the carrier mobility. QSSPC measures the conductivity of the wafer using an RF inductance bridge [27]. A metal coil is placed close to the wafer under test and an RF current is fed through the coil. The alternating magnetic field of the coil induces eddy currents in the wafer. The loss of energy due to the induction of eddy currents is proportional to the wafer's conductivity. The excitation source in QSSPC is a flash lamp with a slowly decaying optical power, the decay being slow enough that the wafer's excess free-carrier population is always in equilibrium with the excitation (hence the reason the technique is referred to as quasi-steady state). The photoconductivity is monitored as the lamp power decays, and with knowledge of the excitation rate the lifetime may be extracted.

Our work is based on free-carrier absorption method. Free carriers are generated by the light source and measured by monitoring the transmission of the infrared light source through the semiconductor material block. The typical configuration of the pump source and the probe source allows the probe to check the area of uniform pump intensity, thereby uniform carrier density. This is achieved by making the pump beam radius much larger than the probe radius. Free carriers absorb infrared light sources in proportion to their density, thereby providing direct detection of free carriers. Due to the generation and recombination of free carriers, this population has changes, so that the lifetime of the semiconductor can be measured.

Frequency-domain FCA is typically referred to as *modulated free-carrier absorption* (MFCA), and involves exciting the sample with a modulated optical source and demodulating the resultant probe signal and extracting the lifetime from the signal's frequency-dependence. Huldt [28] did an experiment which may be one of the earliest Frequency-domain FCA work. His work, using a tungsten strip as the pump, a monochromator set to emit light at a wavenumber of 900 cm$_{-1}$ to derive probe beam, showed that the transmitted power of the probe beam changes by sweeping modulation frequency and people could use the change to predict the lifetime. He measured a lifetime of 165 μs with this technique. Huldt's method was improved in sensitivity by Nilsson [29] who also provided a general mathematical solution to the 1D continuity equation for a square-wave excitation, which is a complete description of the free-carrier recombination in the semiconductor. The minimum lifetime that could be measured by these techniques was limited by the excitation bandwidth of the setup, which is set by the speed of the mechanical chopper.

Sanii et. al [30,31] may finish the first modern version of the MFCA technique, who used a He-Ne laser emitting at 632 nm as pump modulated by an electro-optic modulator and another He-Ne laser emitting at 3.39 μm as probe. Sanii et al. also provided a solution to the 1D continuity equation which is far more algebraically complicated than that of Nilsson. In principle, by fitting the MFCA signal as a function of modulation frequency to this model it is possible to extract the bulk recombination lifetime, surface recombination velocity and diffusion coefficient. In Zhang and Li's work, the diffusion coefficient can be extracted by varying the separation of the pump and probe beams [32], which proved that the phase of the probe signal with respect to the excitation signal grows linearly with separation distance, the slope being proportional to the inverse square root of the diffusion coefficient when the pump and probe are sufficiently separated.

Chapter 3 also includes the derivation of it. Ren et al. extended the 1D diffusion model that considers only diffusion and recombination along the axis of the wafer to three dimensions [33]. Their 3D model is an analytic solution to the continuity equation in three dimensions, accounting for diffusion along the axis of the wafer and parallel to the wafer surface. Their model can be used to fit experimentally measured data and extract the bulk lifetime, surface recombination velocity, and diffusion coefficient simultaneously. The model presented by Ren et al. is very algebraically complicated and written in terms of integrals that don’t yield a closed-form solution. Dr. Kevin M.W. Boyd derived a 3D model in his thesis [34] that is general but also much more compact and usable than Ren’s model. This experiment is guided by his model which is introduced in chapter 3.

2. Theoretical Background

2.1. Absorption in Semiconductors

In order to measure the lifetime of semiconductors, electrons and holes are raised into the conduction band and valence band, and they are observed to change with time or modulation frequency. Electrons and holes are excited by interband absorption into conduction band and valence band, and their population is affected by intraband absorption which is proportional to the density of carriers in the conduction band or valence band, so its measurement gives direct access to the population density of free-carriers. A simplified energy band diagram for an indirect bandgap semiconductor, like silicon, is shown in Figure 2.1, which illustrates interband and intraband absorption processes.

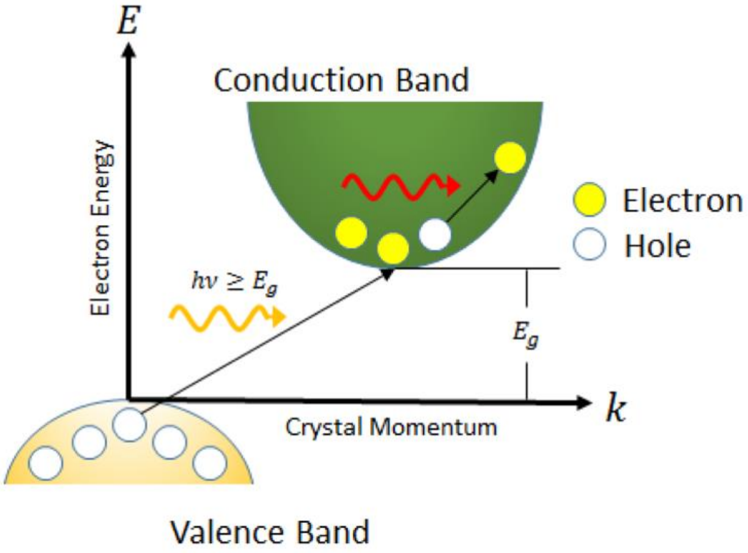

Figure 2.1. Diagram of band-to-band and free carrier absorption processes in an indirect bandgap semiconductor [34].

As for the interband, we also call it band-to-band absorption, which occurs when light is absorbed by a semiconductor to promote an electron from the valence band to the conduction band, leaving behind a hole in the valence band. The light must have energy greater than the bandgap of the semiconductor to make band-to-band absorption occur. In our experiment, we use silicon as the tested sample which has a bandgap of 1.1 eV. From the equation $\lambda = \frac{1.24}{E_g}$, the cut-off wavelength of silicon is around 1100 nm. Silicon is an indirect bandgap semiconductor, so the valence and conduction band edges are not aligned in crystal momentum (Figure 2.1). Since the momentum of light is small, it is necessary to collide with phonons to maintain the momentum to excite electrons to the conduction band in the indirect semiconductor. The requirement for additional quasiparticles to promote the transition reduces the probability of its occurrence, so the absorption coefficient in the indirect band gap is much smaller than that of direct band gap semiconductors (such as GaAs).

When it comes to intraband absorption, which occurs when a free electron or hole absorbs light and is promoted to a higher energy state within the same band, we usually call it free-carrier absorption (FCA) since free-carriers are involved during this process. The energy dispersion in the conduction or valence band is parabolic, so a transition to higher energy states requires a momentum-conserving collision, which may be lattice scattering, electron-hole scattering or scattering from a charged impurity [35]. The classical description of the FCA coefficient α_{FCA} is given by the Drude theory of conductivity [36]:

$$\alpha_{FCA} = \frac{q^3\lambda^2}{4\pi^2\varepsilon_0 c^3 \mathscr{n}}\left[\frac{n}{m_n^{*2}\mu_n} + \frac{p}{m_p^{*2}\mu_p}\right] \tag{2.1.1}$$

where q is the fundamental electron charge, λ is the wavelength of light being absorbed, ε_0 is the permittivity of free space, c is the speed of light, $\mathscr{n}$ is the refractive index of the semiconductor, $m_n{}^*$ and $m_p{}^*$ are the electron and hole conductivity effective masses, respectively, μ_n and μ_p are the electron and hole mobilities, respectively, and n and p are the concentrations of free electrons and holes, respectively. In our work, we generate the free electrons and holes in a one-to-one ratio, which means n=p. Taking this into account, we can write Equation 2.1.1 in terms of the free-carrier absorption cross section σ_{FCA}, which is helpful:

$$\alpha_{FCA} = \sigma_{FCA} n \tag{2.1.2}$$

Equation 2.1.2 shows that the free-carrier absorption coefficient is proportional to a material constant and the free-carrier density. Generally, σ_{FCA} varies with n since the carrier mobilities are dependent on the carrier density [37]. The Drude model, a simplification of a more general model derived from perturbation theory that describes FCA in terms of scattering from acoustic phonons [38] underestimates the value of σ_{FCA}, which is well known in the literature [39]. There are other contributions due to scattering from optical phonons, scattering between electrons and holes, and scattering from ionized impurities (i.e. donor/acceptor atoms) in the material [35,40,41]. FCA is a tool to experimentally access n and a signal measured that is proportional to n is more important than the physics of FCA when taking the aim of this work into account.

2.2. Recombination in Semiconductors

When band to band absorption occurs, a hole can be left in the valence band when an electron is pumped into the conduction band. Due to thermal equilibrium, the generation and recombination of free-carriers share the same rate. Recombination lifetime is a parameter to show the efficiency of recombination, which is the average time over which a population of carriers above the thermal equilibrium concentration recombine. In the experiments, we measure effective lifetime τ to present the total lifetime and here is an equation showing the constant of effective lifetime:

$$\frac{1}{\tau} = \left[\frac{1}{\tau_{rad}} + \frac{1}{\tau_{Aug}} + \frac{1}{\tau_{SRH}}\right] + \frac{1}{\tau_s} \quad (2.1.3)$$

where τ_{rad}, τ_{Aug}, τ_{SRH}, and τ_s are the radiative, Auger, Shockley-Read-Hall (SRH), and surface lifetimes, respectively. Processes of these recombination are illustrated in Figure 2.2. Equation 2.1.3 is a rate equation stating that the total rate of recombination is just the sum of the rates from the contributing recombination mechanisms. Shorter lifetimes represent faster rates of recombination, and dominate the overall contribution to recombination. We use τ_b to present the lifetime in square brackets and call it the bulk lifetime, which is recombination that occurs within the volume of the crystal. The surface lifetime is due to recombination via trap states at the semiconductor's surface.

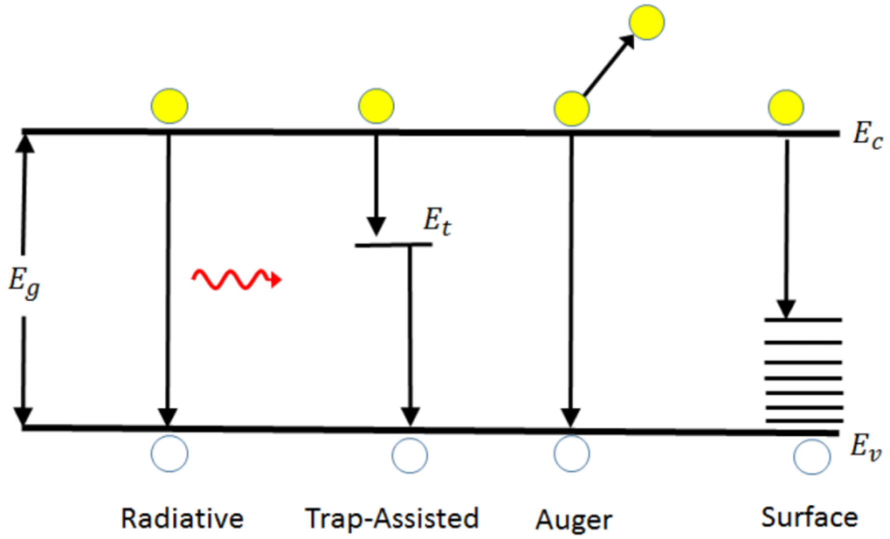

Figure 2.2. A simplified energy band diagram illustrating the fundamental recombination processes in a semiconductor [34].

2.2.1. Radiative, Auger and SRH Recombination

Radiative recombination, or band-to-band recombination, is the reverse process of photon absorption, where an electron drops back down to valence band and radiates a photon; therefore, this type of recombination is how light-emitting diodes or diode lasers create light. These photons contain the same or less energy than those initially absorbed due to the energy lost during the mechanism in indirect semiconductors like silicon. Therefore, radiative recombination plays a more major role in direct band semiconductors, where no change in momentum but only in energy happens because the edges of the valence and conductions bands are aligned in momentum space.

Because of the difference between indirect semiconductor like silicon and direct semiconductor like GaAs, the rate constant for a direct bandgap semiconductor is much larger than that of an indirect bandgap semiconductor. For example, GaAs has B=2x10^{-10} cm^{3}s^{-1} whereas for silicon it is B=1x10^{-14} cm^{3}s^{-1}, and there is a difference of four orders of magnitude [13] which can cause a huge difference in the lifetime. If we choose a background doping level of N_d=10^{16}cm^{-3} and assuming carrier injection is small (n→0), the radiative lifetime in GaAs is about 500 ns, whereas for silicon it is about 10 ms.

The radiative recombination lifetime τ_{rad} can be written as [42, 43]:

$$\tau_{rad} = \frac{\Delta n}{R_r} = \frac{1}{B_r(n_0 + p_0 + \Delta n)} \tag{2.2.1}$$

where R_r is the radiative recombination rate and B_r is rate constant, n_0 and p_0 are the equilibrium carrier densities and Δn is the remaining charge neutrality.

Auger recombination is also caused by an electron recombining with a hole directly, which is similar to that of the radiative recombination. The difference is that in Auger recombination, the energy is given to a third carrier which is excited to a higher energy level without moving to another energy band instead of light. The third carrier normally loses its excess energy to thermal vibrations after the interaction, which makes Auger recombination only significant in non-equilibrium conditions at very high carrier density and is difficult to occur since the third particle would have to begin the process in the unstable high-energy state. Auger recombination causes LED efficiency droop, which is a reduction in the radiative efficiency at high current densities [44].

The Auger lifetime τ_{Aug} is given by [42]:

$$\tau_{Aug} = \frac{\Delta n}{R_A} = \frac{1}{n^2 C_n + 2n_i^2\left(C_n + C_p\right) + p^2 C_p} \tag{2.2.2}$$

where C_n and C_p are the Auger capture probabilities and n_i is the intrinsic carrier density.

Shockley-Read-Hall (SRH) recombination, which is also called trap-assisted recombination, is named after William Shockley, William Thornton Read and Robert N. Hall [13,45]. This type of recombination describes the process in which electrons transitioning between bands pass through a new energy state within the band gap created by dopants or defects in the crystal lattice, which is called a trap. Unlike radiative recombination, SRH is the main recombination process in indirect bandgap materials (such as silicon) because the difference in momentum between carriers can be absorbed by traps. However, when the injection level is very low, resulting in low carrier density in the direct band gap semiconductor, SRH recombination may also be dominant. In addition, in semiconductors with high trap density such as perovskites, SRH recombination is also the main recombination.

Under steady-state condition, we can write SRH recombination rate as:

$$R_{SRH} = \frac{np}{\tau_n(p + p_t) + \tau_p(n + n_t)} \tag{2.2.3}$$

and the average lifetime for electrons and holes can be written as:

$$\tau_n = \frac{1}{B_n N_t} \tag{2.2.4}$$

$$\tau_p = \frac{1}{B_p N_t} \tag{2.2.5}$$

2.2.2. Surface Recombination

Different from the recombination mechanisms discussed above that are considered as bulk recombination, which occurs within the volume of the crystal, surface recombination, as the name suggests, occurs at the surface. Surface recombination is SRH recombination at the surface of a semiconductor, which occurs when traps at or near the surface or interface of the semiconductor form due to dangling bonds caused by the sudden discontinuation of the semiconductor crystal. Surface recombination is characterized by surface recombination velocity which depends on the density of surface defects [46]. Because of the collection and extraction of free carriers at the surface, surface recombination may be the dominant mechanism of recombination in solar cells. In some applications of solar cells, a layer of transparent material with a large band gap, also known as a window layer, is used to minimize surface recombination. For example, an Al doped ZnO window layer is applied in the CIGS solar cell, which serves as a transparent conducting oxide to collect and move electrons out of the cell while absorbing as little light as possible. Besides that, passivation techniques are also employed to minimize surface recombination [47].

3. Theoretical Equations

This chapter presents the derivation of theoretical equations used in this work, including lifetime calculation with Lorentzian fitting model, generalized semiconductor probe/pump equation presenting the carrier distribution in time domain, and phase equation from carrier distribution equation at a certain assumption. All the equations are from Dr. Rafael N. Kleiman and Dr. Kevin M. W. Boyd's work and will be the guidance of the simulation process which is discussed in chapter 5.

3.1. Lifetime Calculation

3.1.1. Time, Frequency, and Quasi-Steady State Domains

Equation 3.1.1 shows a differential equation to present time rate-of-change for free carriers in a semiconductor:

$$\frac{\partial n}{\partial t} = g(t) - \frac{n}{\tau} \tag{3.1.1}$$

where n is the concentration of electrons above the thermal equilibrium concentration, τ is the recombination lifetime and $g(t)$ is the volumetric generation rate of free carriers. Experimentally, n is measured in the time, frequency, or steady-state/quasi-steady regimes and the way to monitor n and temporal nature of $g(t)$ are different.

A pulsed laser with pulse-width << τ is used in time domain studies to excite n near-instantaneously, and then monitor n over time as it decays back to equilibrium [48]. Under these circumstances, a Dirac-delta function in time can be applied to estimate $g(t)$, and Equation (3.1.1) can be rewritten as $\frac{\partial n}{\partial t} = -\frac{n}{\tau}$ when taking the initial condition $n(0)=n_0=N_0$ into consideration, where N_0 is the number of photons absorbed from the laser pulse. The solution to this equation is:

$$n = n_0 e^{-\frac{t}{\tau}} \tag{3.1.2}$$

Equation (3.1.2) shows that n has an exponential decline from an initial concentration n_0 to 0 with a decay constant equal to the recombination lifetime. Hence, we can obtain τ by fitting this exponential function. The only physical quantity to measure is n, which can be found by measuring another physical quantity proportional to it. In the μ-PCD technique this quantity is the power of microwaves reflected from the semiconductor, which is related to photoconductivity. In the free-carrier pump/probe technique this quantity is the absorption of an optical probe beam.

In frequency domain studies, $g(t)$ describes a harmonically varying excitation of angular frequency ω, which leads to a harmonically varying n. In frequency domain, the signal amplitude is a complex number consisting of the real part, the signal component in phase with the excitation and the imaginary part, the signal component 90° out of phase with the excitation. We use $N(\omega)$ and $G(\omega)$ to present the complex amplitudes of the free-carrier population and generation rate, respectively. In this case, we can rewrite n and $g(t)$ in their harmonic form: $n=N(\omega)e^{i\omega t}$ and $g(t)=G(\omega)e^{i\omega t}$. By substituting n and $g(t)$ into (3.1.1), we can obtain:

$$N(\omega) = \frac{G(\omega)\tau}{1 + i\omega\tau} \tag{3.1.3}$$

Equation (3.1.3) is the frequency response of the free-carrier population under a harmonic excitation which is a Lorentzian function. It matches the experimental measurement in this work which is measured in frequency domain. In our experiment, the modulation frequency of the excitation is swept while the value of $N(\omega)$ is computed from the data measured by the IR Camera.

Then we can extract τ by fitting the computed $N(\omega)$ with the shape of (3.1.3).

In steady-state or quasi-steady state lifetime measurements, $g(t)$ is a constant or changes slowly and the excitation with the constant $g(t)$ is used to measure n. In this case, the excitation varies slowly enough making sure that n is always in equilibrium with it. Taking this into account, we can have a special case of Equation (3.1.3), where $\omega\tau \ll 1$:

$$n = G\tau \tag{3.1.4}$$

Equation (3.1.4) shows that the free-carrier population measured under a constant generation rate G is directly proportional to τ, in which n is measured experimentally and G is known, allowing τ to be extracted. In this work, measurement of lifetime is performed exclusively in the frequency or quasi-steady state regimes.

3.1.2. The Effective Lifetime

The bulk lifetime τ_b can have more interest from experimenter when measuring recombination lifetime, particularly the Shockley-Read-Hall lifetime, where we can obtain the information about the nature of defects in a semiconductor [28]. Generally speaking, the actual lifetime measured experimentally consists of the bulk lifetime and surface lifetime. As has been discussed, we measure the lifetime in quasi-steady regimes and in frequency domain. Dr. Kevin M.W. Boyd has discussed in his thesis that the effective lifetime measured in quasi-steady and the lifetime measured in a time/frequency domain study are only equivalent in the limit of slow surface recombination velocity ($S \leq 1000$ cm/s) [34]. When surface recombination goes to zero both lifetimes are equivalent to the bulk lifetime. A distinction is made between the two, with τ_{qss} being the lifetime measured in quasi-steady state conditions, and τ being measured via the roll-off frequency of (3.1.3). In this section I'll present some work from Dr. M.W. Boyd on examining how it differs for the quasi-steady state and roll-off measurement approaches.

If we take the 3-dimensional nature of carrier generation and diffusion into consideration, we can rewrite Equation (3.1.1) to a more general equation describing the time-dependent excess electron concentration n in a semiconductor as:

$$\frac{\partial n(r,z,t)}{\partial t} = D\nabla^2 n(r,z,t) - \frac{n(r,z,t)}{\tau_b} + g(r,z,t) \tag{3.1.5}$$

where D is the diffusion coefficient, τ_b is the bulk recombination lifetime, and g is the volumetric generation rate of free-carriers. Equation 3.1.5 is the 3D continuity equation for electrons in cylindrical coordinates and states that the time rate of change of the electron population in a differential volume of semiconductor material is equal to the sum of the net rates at which carriers diffuse into the volume, recombine inside the volume, and are generated due to optical excitation. Since electrons and holes are generated and recombine in equal concentrations, we can ignore the drift effects and maintain charge neutrality. A consequence of electrons and holes being generated in equal concentrations is that the carrier diffusion becomes ambipolar [49]. In silicon, electron is majority carrier with higher mobilities than that of hole, which results in a higher diffusion coefficient for electrons [35]. Therefore, electrons diffusing faster than holes, leading to a spatial charge imbalance and bringing the carriers back together due to Coulombic attraction. Eventually, it is more likely for the carriers to diffuse together with a diffusion coefficient in the middle of the value for electrons and holes. The result of ambipolar diffusion is that there is no need to consider the transport of electrons and holes separately. The equations describing electron transport and recombination are the same as those describing hole transport and recombination. Therefore, only $n(r, z, \tau)$ is required to give a complete description of carrier migration and reorganization in real experiments. Therefore, n is interpreted as the density of free carriers, not the density of electrons.

The pump beam diameter is much larger than the diffusion length of free-carriers in most lifetime experiments, permitting a purely 1-dimensional treatment of the continuity equation:

$$\frac{\partial n(z,t)}{\partial t} = D\frac{\partial^2}{\partial z^2}n(z,t) - \frac{n(z,t)}{\tau_b} + g(z,t) \tag{3.1.6}$$

where z is the dimension along the thickness axis of the wafer. We can ignore the surface recombination when the generation rate is uniform along z, thus n and g are independent of position and (3.1.6) reduces to (3.1.1). In this case, we can have solution from Equation 3.1.3. In order to make the discuss more convenient, we define a generalized lifetime $\mathfrak{T}_s = N(\omega)/G(\omega)$. Then we can rewrite Equation 3.1.3 to:

$$\mathfrak{T}_s = \frac{\tau}{1 + i\omega\tau} \tag{3.1.7}$$

Equation 3.1.7 is the idealized case where the surface recombination is ignored and the characteristic lifetime is the bulk lifetime. However, when the surface passivation is imperfect, additional recombination occurs, thereby reducing the surface excess carrier density. This in turn leads to diffusion flux towards the surface, leading to further recombination. Now, this situation becomes more complicated as the absorption distribution of the excitation source is also considered. When the absorption coefficient is high, since most carriers are generated near the surface, the surface recombination effect will be more exaggerated. We can solve Equation 3.1.6 directly by applying surface-recombination boundary conditions at the front and rear surfaces of the wafer to take the situation including surface recombination into account [30]. Then we can obtain equations between the surface recombination velocity at the surface of the wafer, S and diffusion coefficient, which have an analytic solution to this equation in the time domain provided by Luke and Cheng [50]:

$$n(t) = \phi_0 \frac{1-R}{1-Re^{-\alpha\eta W}} \frac{8\alpha\eta e^{-\frac{\alpha\eta W}{2}}}{W} \sum_{n=1}^{\infty} A_n^{lc} e^{-\frac{t}{\tau_n}} \tag{3.1.8}$$

where ϕ_0 is the photon flux per unit area, α is the absorption coefficient of the pump beam, η is the ratio of pathlength through the wafer to the wafer thickness, R is the reflectance of the pump beam, W is the wafer thickness. The factor A_n^{lc} is known as the Luke and Cheng coefficient. The factors τ_n are the series effective lifetimes, given by:

$$\tau_n = (\frac{1}{\tau_b} + \alpha_n^2 D)^{-1} \tag{3.1.9}$$

where factors α_n are given by:

$$\delta_n = \frac{\alpha_n W}{2} \tag{3.1.10}$$

$$cot\delta_n = \left(\frac{2D}{SW}\right)\delta_n \tag{3.1.11}$$

It is noticeable that there is no dependence on z in Equation 3.1.8 because this dependence is averaged out by integrating over the thickness of the wafer. Given that in this work, the data measured by the IR camera is in frequency domain, where generation rate is harmonically varying in time and the complex amplitude of the free-carrier density $N(\omega)$ is measured, we convert $n(t)$ to the frequency domain and writing in terms of $\mathfrak{T}_s$ yields:

$$\mathfrak{T}_s = \frac{8\alpha\eta e^{-\frac{\alpha\eta W}{2}}}{1-e^{-\alpha\eta W}} \sum_{n=1}^{\infty} \frac{\tau_n A_n^{lc}}{1+i\omega\tau_n} \tag{3.1.12}$$

Compared to Equation 3.1.7 which is a single Lorentzian roll-off curve, Equation 3.1.12 takes on a similar form with multiple roll-off terms. The first term is usually much larger than higher order terms and the total decay is effectively a single roll-off parameterized by τ as the first order of Equation 3.1.9. From Dr. Kevin M.W. Boyd's work, an alternative form of Equation 3.1.12 is completely closed-form, which is an elegant algebraic simplification of the solution presented by Sanii [30] that reduces a very complex equation to a much simpler form and is shown as:

$$\mathfrak{T}_s = \frac{L^2}{D((\alpha\eta)^2L^2 - 1)}\left[\frac{\mu + coth\,\frac{\alpha\eta W}{2}}{\nu + coth\,\frac{W}{2L}}\alpha\eta L - 1\right] \tag{3.1.13}$$

where L is the effective diffusion length, D is the diffusion coefficient, α is the absorption coefficient, and μ and ν are dimensionless parameters. L, μ and ν are given by:

$$L = \sqrt{\frac{D\tau_b}{1 + i\omega\tau_b}} \tag{3.1.14}$$

$$\mu = \frac{\alpha\eta D}{S} \tag{3.1.15}$$

$$\nu = \frac{D}{LS} \tag{3.1.16}$$

In order to have a better understanding on the difference between the exact solution for the frequency-domain free-carrier concentration (Equation 3.1.13) and simplified solution in 3.1.7, Dr. Kevin M.W. Boyd compares the two for various surface recombination velocities and absorption coefficients in Figure 3.1 with the wafer parameters of τ_b=100 µs, W=300 µm, and D=16 cm^2/s. The absorption coefficient α and the SRV are varied between low and high values to demonstrate how surface recombination affects the shape of the curve. The exact solution is plotted for a particular set of parameters, and then fitted to the simplified model given by Equation 3.1.7 to determine the effective lifetime.

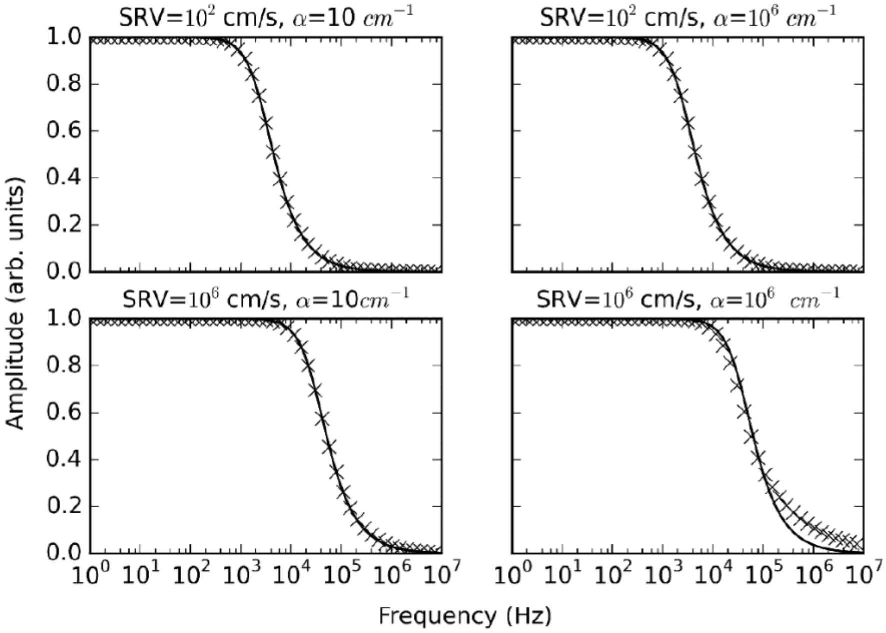

Figure 3.1. Plot of Equation 3.1.13 vs frequency ('x' markers) and a fit to Equation 3.1.7 (solid-line) for various combinations of surface recombination velocity and absorption coefficient [34].

In the case when the absorption coefficient is small, only the first term in the series is dominant and so we can use Equation 3.1.17 to present the effective lifetime.

$$\tau = (\frac{1}{\tau_b} + \alpha_1^2 D)^{-1} \tag{3.1.17}$$

From Figure 3.1, it is noticeable that when both SRV and the absorption coefficient are high, the frequency-response is perturbed from its Lorentzian shape at high frequencies. However, higher order terms in Equation 3.1.13 only contribute to high-frequency regions beyond 200 kHz. From Dr. Kevin M.W. Boyd’s work, the lifetime corresponding to the first term (i.e. the effective lifetime) is τ_1=5.40 μs and the fitted lifetime values by Lorentzian with and without high frequency regions are τ=4.34 μs and τ=4.86 μs, which is closer to the true value [34]. Our work has a test frequency range between 1 kHz to 200 kHz, and during this range, the fit and the actual effective lifetime match well. Therefore, we can use the Lorentzian shape to extract the lifetime by fitting the amplitude of frequency domain carrier density, which is discussed in chapter 5.

3.2. Carrier Radial Distribution Equation

To describe the carrier distribution with pump/probe and QSS-FCA techniques used in our work, Dr. Kevin M.W. Boyd develops a generalized pump/probe equation to describe the signal measured in a generic pump/probe experiment on a semiconductor wafer. The general model is derived from an equation that describes the free-carrier density $n(r, z, t)$ as a function of radial (r) and axial (z) position, and time (t). The equation for $n(r, z, t)$ provides a general description of free-carrier transport and recombination in a semiconductor for an arbitrary set of wafer parameters. The derivation result is:

$$n(r,z,t) = e^{-\frac{t}{\tau_b}} \frac{1}{\frac{t}{\tau_D}+1} e^{\frac{-2r^2}{w^2(\frac{t}{\tau_D}+1)}} \sum_n [A_n^{\alpha x} e^{-\alpha_n^2 Dt} cos\alpha_n z + B_n^{\alpha x} e^{-\beta_n^2 Dt} sin\beta_n z] \qquad (3.2.1)$$

From what has been discussed before, as what has been shown in Equation 3.1.8, the z-dependence can be averaged out in time-domain, Dr. Kevin M.W. Boyd has derived a general solution shown as Figure 3.2.2.

$$n(r,t) = 8g_0\alpha\eta e^{-\frac{\alpha\eta W}{2}}\frac{1}{\frac{t}{\tau_D}+1}e^{\frac{-2r^2}{w^2(\frac{t}{\tau_D}+1)}}\sum_n e^{-(\tau_b^{-1}+\alpha_n^2 D)t}A_n^{lc} \tag{3.2.2}$$

In the tested range in our work, we can use the first term of Equation 3.1.9 (Equation 3.1.17) as the effective lifetime and we can lump the part of $8g_0\alpha\eta e^{-\frac{\alpha\eta W}{2}}A_n^{lc}$ to a constant C, then we can rewrite Equation 3.2.2 to Equation 3.2.3.

$$n(r,t) = Ce^{-\frac{t}{\tau}}\frac{1}{\frac{t}{\tau_D}+1}e^{\frac{-2r^2}{w^2(\frac{t}{\tau_D}+1)}} \tag{3.2.3}$$

where τ_D is the *diffusion time constant*, given by:

$$\tau_D = \frac{w^2}{8D} \tag{3.2.4}$$

Therefore, the time domain carrier distribution is only dependent on τ and D in different combinations, as well as the frequency domain distribution. Equation 3.2.3 is a general description of free-carrier transport in a semiconductor under a Gaussian-shaped excitation beam. The solution is derived by assuming an optical generation rate that is a Dirac-Delta function in time. Equation 3.2.3 cannot be Fourier transformed analytically if we do not apply any limits on the variables, so we have to transform it numerically to obtain the frequency domain data to match the experimental data we get from the camera. In the simulation process which is discussed in chapter 5, we apply the Fast Fourier Transform to Equation 3.2.3 to compute the complex matrix of carrier distribution in frequency domain and fit the curve to compute lifetime and radial distribution coefficient.

In order to make a better understanding on this equation, we attempt to analyze the phase part of the equation. From the work of Luke and Cheng [50], we can obtain equations discussed before.

If we assume $w_{pr}^{w} \gg w_{pu}^{w}$ or $w_{pr}^{w} \gg L^2$, which is met in our experiment, the probe is constant over image plane. Then we can derive that the phase slope is given by:

$$\frac{d\varphi}{dr} = \frac{\sqrt{A-1}}{L\sqrt{2}} \tag{3.2.5}$$

where

$$A = \sqrt{1 + \omega^2\tau^2} \tag{3.2.6}$$

And L is defined as

$$L^2 = D\tau \tag{3.2.7}$$

Equation 3.2.5 is valid when the distance from the beam centre, r > pump beam width w, which illustrates that in the range of r > w, the phase is a linear model and by fitting the phase slope we can compute lifetime and diffusion coefficient. This conclusion is verified by the simulation process discussed in chapter 5.

4. Experimental Apparatus

4.1. Overview

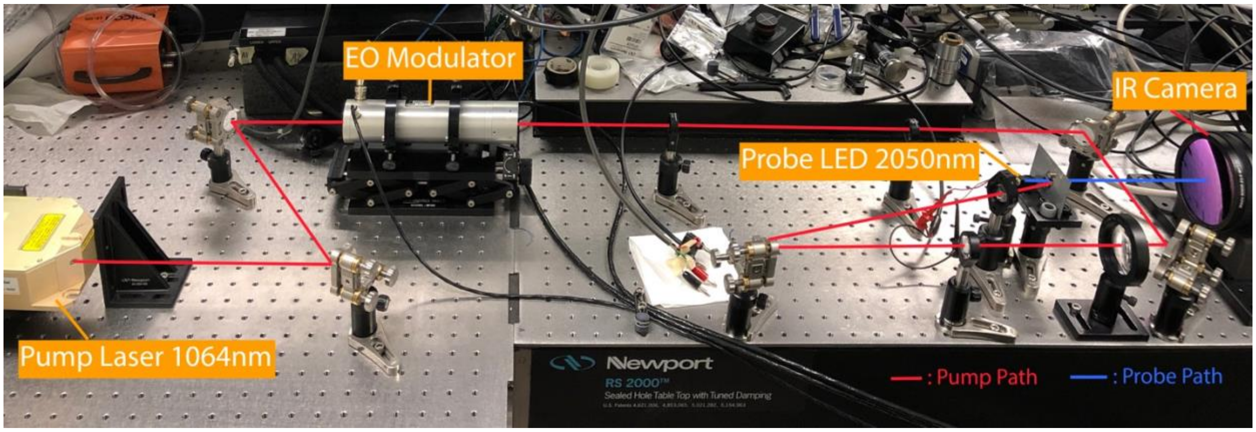

Figure 4.1. Photograph of experimental apparatus. The path of the pump beam and probe beams from source to detector is shown by red and blue lines, respectively.

The system for carrier lifetime and diffusion coefficient measurement consists of a generic pump/probe configuration. We select 1064 nm laser as the pump radiation which can emit photons with energy above the bandgap of silicon and thus generating free electron-hole pairs in the silicon sample. We used a 2050 nm LED as the probe to get an easily-modulated and uniform source with enough power, which can emit radiation that has energy below the bandgap of silicon, and is absorbed primarily by intraband free-carrier absorption. The light with wavelength of 2050 nm can be received and measured by the IR camera used in our experiment. After free electron-hole pairs being generated in the silicon sample by pump beam, the probe beam, with photon energy below the silicon bandgap experiences no band to band absorption but sees the free carrier absorption which follows the function used to modulated the pump beam. Thus, the probe beam passes through the sample and is detected by the IR camera, where we can get the diffusion images. The experimental apparatus is shown in Figure 4.1. The red and blue lines show the path of the pump and probe lasers, respectively, from source to detector. The apparatus can be broken down into three branches: Pump, Probe, and Measurement branches. The individual branches will be described in this Chapter.

4.2. Pump Branch

The pump branch starts from a pump laser source, then the beam is reflected twice by mirrors, after which it goes through an EO Modulator and is modulated. After the modulator, we use two lens groups to shrink the beam and reduce the beam size. The beam radius is around 400 µm after the modulator and can be reduced to less than 90 µm with these four lenses (measured by knife-edge method). Before hitting the sample, the beam is focused by a convex lens of 50.2 mm focal length to obtain the max power and give us usable data at higher frequencies.

The pump laser is a diode-pumped solid-state laser from Laser Quantum. The laser emits 45° polarized 1064 nm radiation with 800 µm beam size and 30 GHz linewidth. The max power of the laser is 1 W and it is operated at half the maximum power in this work. The laser is mounted at an upper platform by three stands as a cooling system. The beam is reflected twice by two adjustable mirrors and is kept at the same height before being guided into the EO-Modulator to reduce the influence of double reflection inside the modulator. The EOM is Model 360-160 from Conoptics Inc and is constructed with Lithium Tantalate (LTA) Pockel's cell, which is built for 1064 nm radiation and supports the full 1 W of the laser. The modulator is driven by Model 25A driver (not shown) from Conoptics, which can create an arbitrary analog signal on the laser beam with the bandwidth up to 25 MHz. The EOM obtains sinusoidal signal from Keysight 33500B waveform generator to modulate the pump beam at frequencies from 1 kHz to 200 kHz. After being modulated by the EOM, the pump beam is guided into an optical system consisting of 4 convex lenses and two mirrors for shrinking the beam. Based on the laser manual, the beam size should be around 800 μm; taking the influence by the EOM into account, the beam size can be even bigger and is larger than 1 mm from our measurement. The beam size measurement method is knife-edge, which is introduced in the fourth part of this chapter. In order to shrink the beam and obtain enough power to generate clear images at the end, we made two lens group to make the beam smaller and two mirrors to change the light path, increasing space utilization. The focal lengths of the lenses used in the lens groups are 200 mm, 50.2 mm, 100 mm and 38.1 mm, respectively. The reduced beam then is reflected by another mirror to a 50.2 mm convex lens before hitting the sample.

4.3. Probe Branch

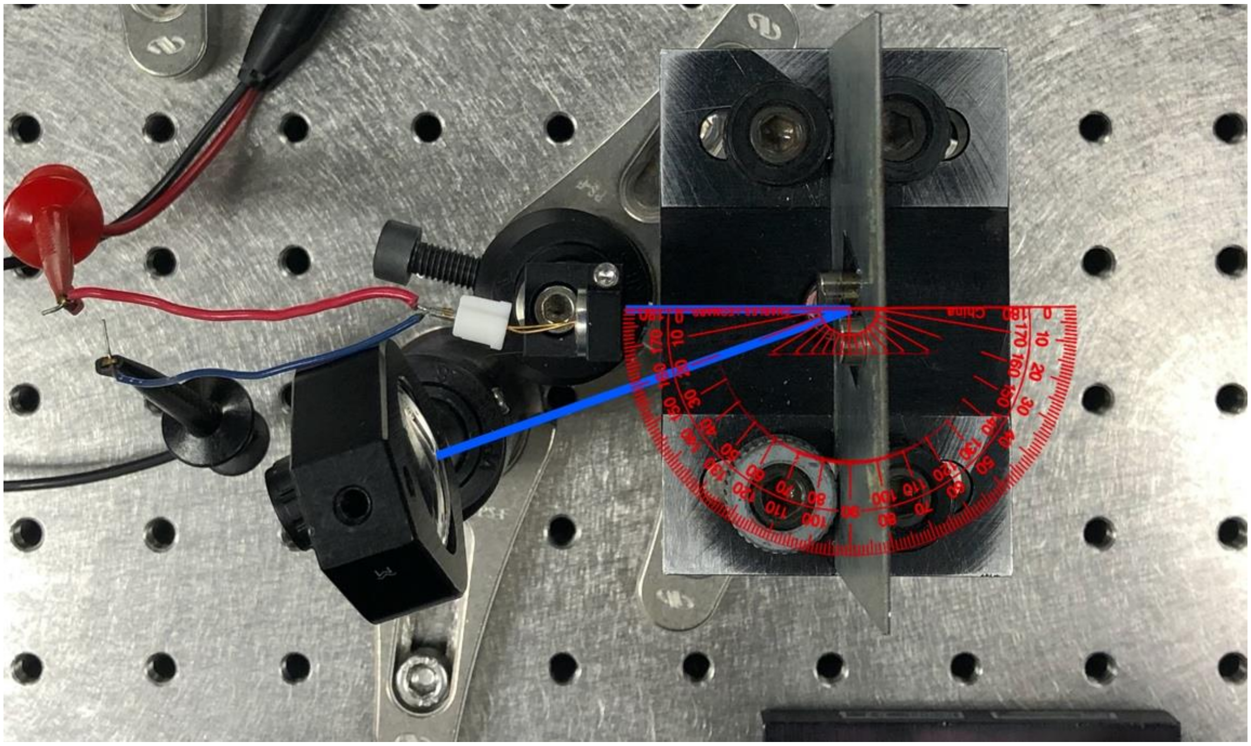

Figure 4.2. Vertical view of the probe branch.

The probe beam is from THORLABS LED2050P which is composed of heterostructures (HS) grown on a GaSb substrate and can emit 2050±50 nm radiation at the output. The LED is driven by ILX Lightwave LDX-3525B precision current source from Newport with a bandwidth of 150 kHz, which can modulate the probe beam by obtaining the sinusoidal signal also from Keysight 33500B waveform generator at frequencies from 1 kHz to 200kHz, but at 5 Hz more than each of the pump channel. The probe beam is guided to the sample directly to reduce the power loss and to be imaged by the camera, which can make it difficult to guide the pump to the sample directly, thus making the diffusion images elliptical. In order to reduce that distortion, we use the last mirror to keep the pump path far enough from the sample before hitting and having a relatively small angle, which is small enough to give us circular diffusion images. Figure 4.2 shows the vertical view of the probe branch and the angle between the probe beam and pump beam is around 20 degrees when we make the pump beam go through the center of the focus lens and hit the center of the silicon sample.

4.4. Measurement Branch

The measurement branch of the final system is an Infrared Thermographic Camera ImageIR 8300 form InfraTec with detection range from 2 μm to 5 μm. The detector format of this camera is 640 * 512 IR pixels and the length of each pixel is 14 μm. ImageIR 8300 is an InSb camera, which is designed to measure temperature with a large temperature measuring range from -40 to 300 ℃. There camera is configured as a lock-in thermography system which is used to measure the amplitude and phase of small temperature changes at a given reference frequency, returning the complex temperature as a result. This camera system is calibrated in units of temperature change, which is proportional to changes in the IR intensity of the probe beam. We have verified that the intensity changes reported by the camera system are proportional to the intensity changes in our experiment by measuring the returned signal from the camera with different probe intensities. Therefore, we can regard the reported temperature changes from the camera system as a measure of changes in the probe intensity which is also a measure of changes in the free carrier density through Equation 2.1.2. For the lens used for the camera, we select a telephoto lens with 100 mm focal length. Then we feed sine signals to pump and probe beam at 70 different frequencies from 1 kHz to 200 kHz. As the recombination lifetime determines the response rate of minority carrier density, the carrier diffusion can fail to response to optical generated carriers at high frequency which makes the diffusion spot small at high frequency. As frequency goes down, the spot broadens and stops changing at low frequency where diffusion length dominates the shape. We regard the frequency in the range of $\omega\tau < 1$ as low frequency where the spot shape is only governed by diffusion length and the frequency in the range of $\omega\tau > 1$ as high frequency where diffusion starts losing the domination of shape and the spot shape starts shrinking as the frequency goes up and is mostly like the beam shape itself. We obtain the complex data from camera, therefore the amplitude and phase data of carrier density data both follow this theory. The carrier density of all the three frequency regions ($\omega\tau < 1, \omega\tau = 1, \omega\tau > 1$) have a different dependence on D and τ, which determine D and τ together. Figure 4.3 shows spot images from camera at several frequencies in the tested frequency range from 1 kHz to 200 kHz.

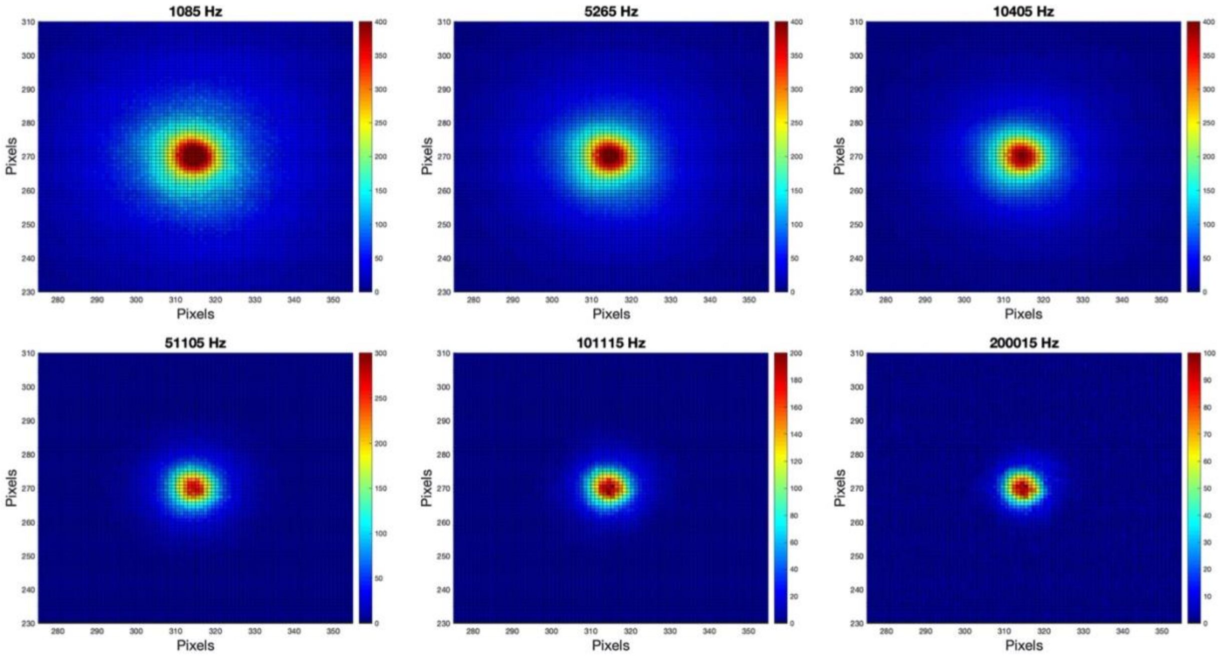

Figure 4.3. Spot images from camera at several frequencies in the tested range from 1 kHz to 200 kHz.

Besides the camera, we perform two additional calibration measurements in this experiment. The 360-160 EOM used to modulate the pump beam can have resonance at some frequencies, which can influence the results. In order to correct for them, we build a resonance checking system to calculate the influence of resonance at each frequency and then cancel them out. We select model 2033 IR photoreceiver from New Focus and link it to SR830 DSP lock-in amplifier, where we can obtain the magnitude and phase of the pump beam after the EOM at each frequency.

As mentioned before, the laser beam size is around 800 μm from the head and can be a little bit bigger after passing the EOM; therefore we built a knife-edge system which is shown in Figure 4.4 to measure the beam size and use lens groups to make it smaller. The knife-edge branch consists of Newport CMA-12CCCL linear actuator holding a perforated plate where we attach a knife to cover half of the hole with magnets. A Newport ESP300 universal motion controller is used to drive the actuator with 50 nm precision. New Focus model 2033 IR photoreceiver is also used for pump laser measurement and is linked to gentec-eo power meter to obtain the power after the knife-edge system.

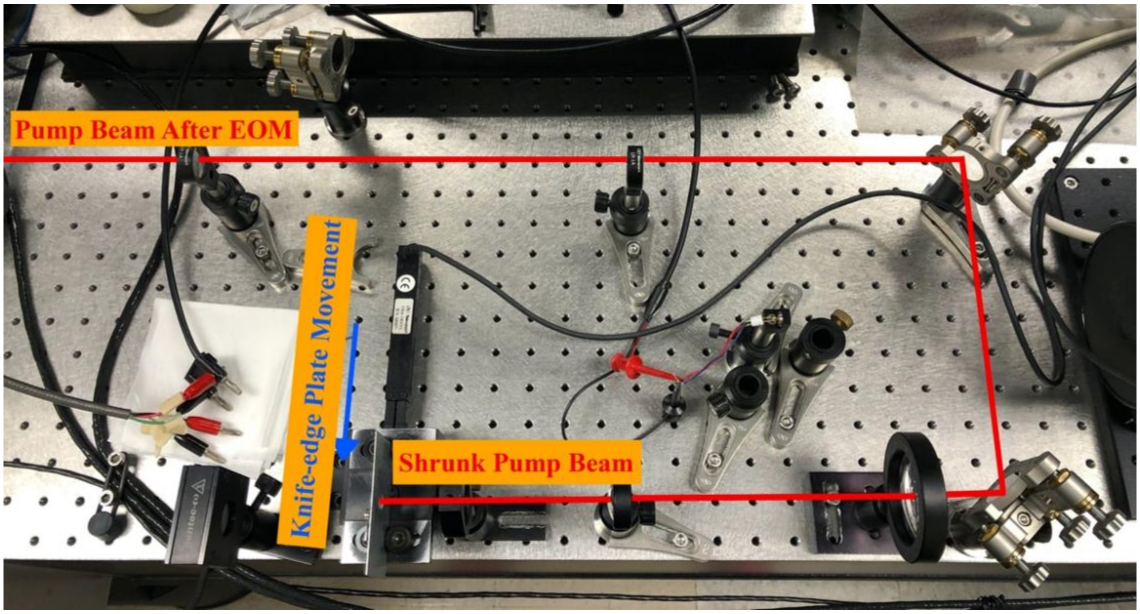

Figure 4.4. Knife-edge branch to measure the beam size of the pump beam and prove that the pump laser is Gaussian-shaped excitation which can be applied to the theory.

4.5. Experimental Methodology

In this part, the experimental methodology is discussed. After turning on the equipment, our first step is to modulate the pump beam. A sine wave with DC offset is generated and outputted from Keysight 33500B waveform generator, being fed into a Conoptics Model 25A Driver. By setting a proper value for the DC bias voltage on the Model 25A Driver, the sine wave signal can be amplified and fed into the EOM, which modulates the pump laser beam. The parameter setting for the waveform generator is 2.4 Vpp for amplitude and 1.2 V for offset. We select this setting by analyzing the curve of EOM and the proper bias of it, then we adjust them and measuring the received temperature from the camera. The received power doesn’t increase any more when the modulation amplitude goes up to 2.8 Vpp, but we don’t use as much power as we can because the camera software can suffer from signal delay when the received power is excessive, influencing the diffusion images. As for the probe beam, we feed a sine wave signal of 1.6 Vpp amplitude and 0.8 V offset from Keysight 33500B waveform generator to ILX Lightwave LDX-3525B precision current source to modulate the probe LED. The parameter setting is chosen by the same method as that of the pump beam. This experiment is run at frequencies from 1 kHz to 200 kHz in logarithmically spaced steps and the frequency of the signal fed to the probe beam is 5 Hz more than that of the pump beam. Figure 4.5 illustrates the function settings for probe and pump beam at one tested frequency.

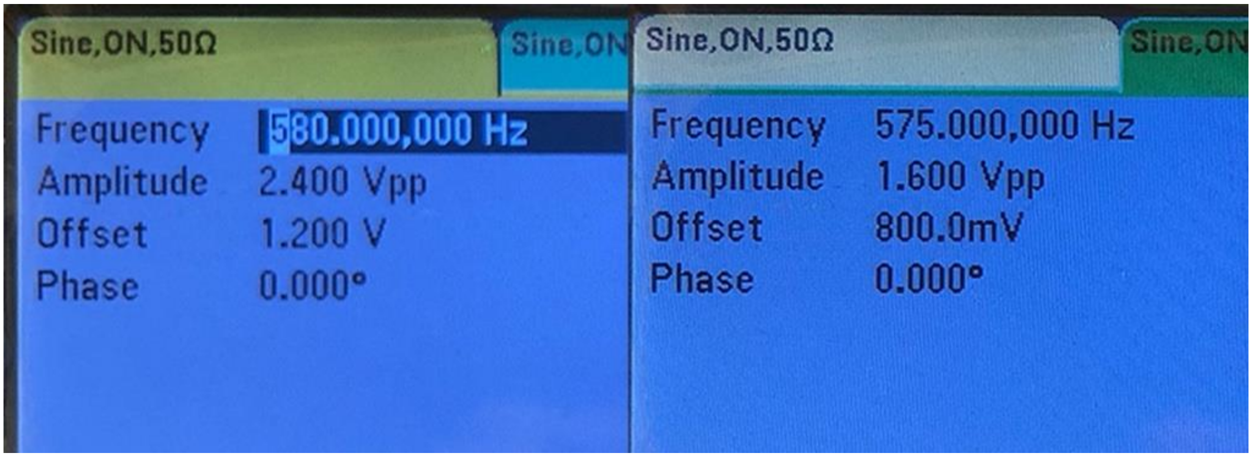

Frequency 580.000,000 Hz
Amplitude 2.400 Vpp
Offset 1.200 V
Phase 0.000°

Frequency 575.000,000 Hz
Amplitude 1.600 Vpp
Offset 800.0mV
Phase 0.000°

Figure 4.5. Settings for pump beam (left) and probe beam(right).

As shown in Figure 4.5, there is a 5 Hz difference between the pump beam and probe beam. The camera used in this work can only have the framerate up to 20 Hz, and the frequency we used in this work to modulate the pump and probe can go to 200 kHz, which the camera can't response to. However, when the pump and probe hit the sample, signals from pump and probe are convolved. If we use ω_{pu} and ω_{pr} to present the pump and probe frequencies, respectively and $\omega_{pu} = \omega_{pr} + \Delta\omega$. From the product-to-sum identities:

$$2sin\theta sin\varphi = cos(\theta - \varphi) - cos(\theta + \varphi) \qquad (4.5.1)$$

then substitute ω_{pu} and ω_{pr} into Equation 4.5.1, we can obtain two function parts: $\cos{(\omega_{pu} - \omega_{pr})t} = \cos{(\omega_{pr} + \Delta\omega - \omega_{pr})t} = \cos{(\Delta\omega)t}$, which can be detected by the camera and $\cos{(\omega_{pu} + \omega_{pr})t} = \cos{(\omega_{pr} + \Delta\omega + \omega_{pr})t} = \cos{(2\omega_{pr} + \Delta\omega)t}$, which will be ignored by the camera because ω_{pr} is way higher than the response range of camera.

After finishing the settings of the experimental system, the settings on the camera software should be done before running the system. We removed all the filters by selecting filter 0 in the camera setting, which can be opened by pressing F5 or right clicking when selecting the image interface, to obtain as much power as we can and match the lock-in frequency to the frequency difference between probe and pump. Figure 4.6 shows the interface of the camera software with the settings used in our work. At the end of measuring, we can obtain the raw data from the software and transfer them to ascii data for simulation steps, which are discussed in chapter 5.

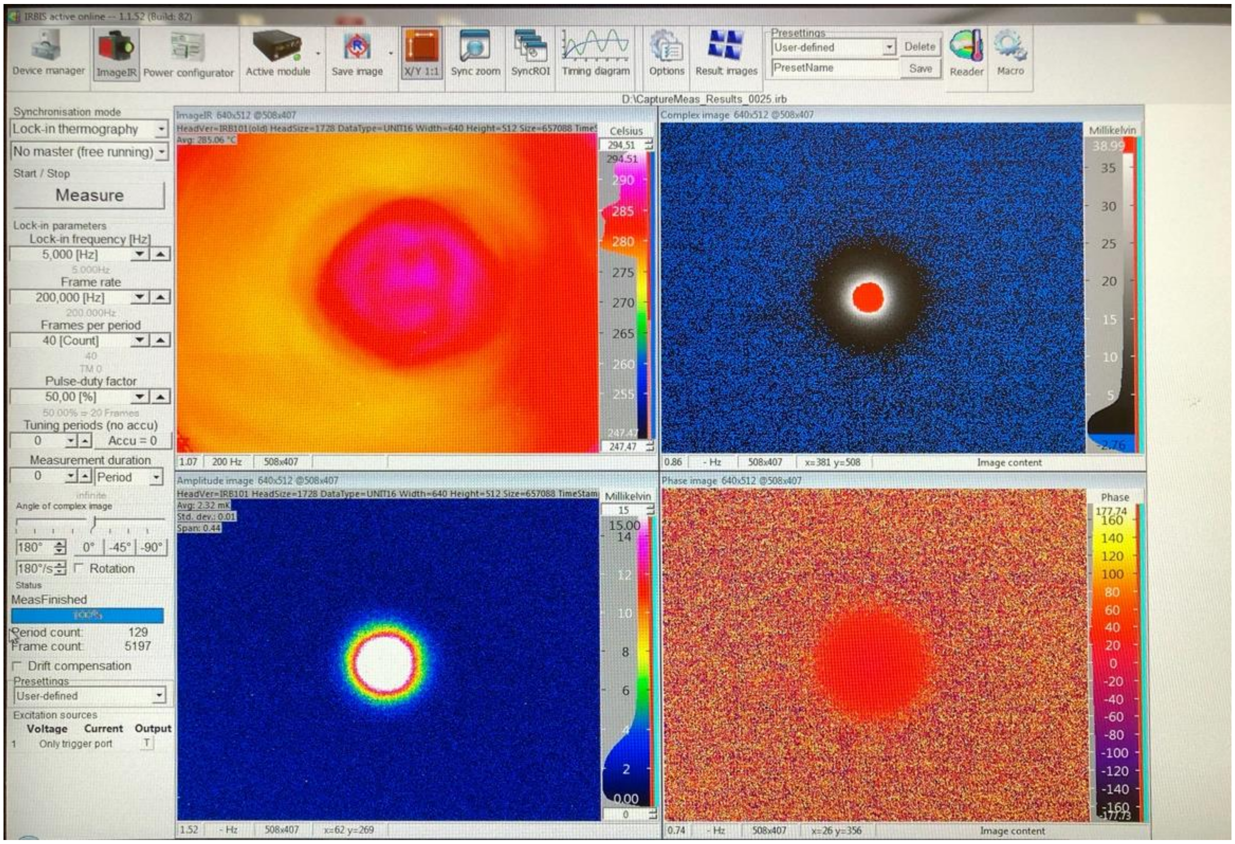
IRBIS active online -- 1.1.52 (Build: 82)

D:\CaptureMeas_Results_0025.irb

Synchronisation mode: Lock-in thermography

No master (free running)

Lock-in parameters

Lock-in frequency [Hz]: 5,000 [Hz]

Frame rate: 200,000 [Hz]

Frames per period: 40 [Count]

Pulse-duty factor: 50,00 [%]

50.00% = 20 Frames

Tuning periods (no accu): 0 Accu = 0

Measurement duration: 0 Period

infinite

Angle of complex image: 180° 180°/s ☐ Rotation

Status: MeasFinished

100%

Period count: 129

Frame count: 5197

☐ Drift compensation

Presettings: User-defined

Excitation sources

	Voltage	Current	Output
1	Only trigger port		T

ImageIR 640x512 @508x407

HeadVer=IRB101(old) HeadSize=1728 DataType=UNIT16 Width=640 Height=512 Size=657088 Time

Avg: 285.06 °C

Amplitude image 640x512 @508x407

HeadVer=IRB101 HeadSize=1728 DataType=UNIT16 Width=640 Height=512 Size=657088 TimeStam

Avg: 2.32 mK

Std. dev.: 0.01

Span: 0.44

Figure 4.6. Camera software interface with experimental settings.

The measurement in the experiment is almost entirely automated and controlled via a custom instrument control Application Programming Interface (API) mostly written by my colleague, Dr. Kevin M.W. Boyd in Python. By using GPIB and USB connections, this API gives an experimenter complete control over laboratory instruments including control of laser power, modulation amplitude and frequency, positioning of flipper mirrors, and data acquisition all occur remotely and automatically. Switching in new samples and changing the setups to the resonance measuring system or knife-edge system are the only parts of the experiment that requires human intervention.

Resonance data of the EOM and the beam profiles are also needed in the simulation steps. We obtain the resonance data by using the resonance measurement system discussed before. The API can also obtain the data from SR830 lock-in amplifier automatically and these data will be used in the simulation process to get rid of the influence from resonance, which is discussed in chapter 5. By controlling the linear actuator in the knife-edge system and record the points of the laser power from max to zero, which can be fitted by Gaussian distribution [51], we can have an idea on the beam waist of the laser, and confirm that the laser used in this experiment follows Gaussian distribution, which allows us to extract the beam radius for quantitative calculations. The fitting results illustrated in Figure 4.7 are for pump beam before and after beam shrinking lens groups. The pump beam follows the Gaussian distribution before and after lens groups and the beam size is decreased by a factor of 12 from 1075 μm to 88 μm, which matches the focal lengths of the lenses in the groups.

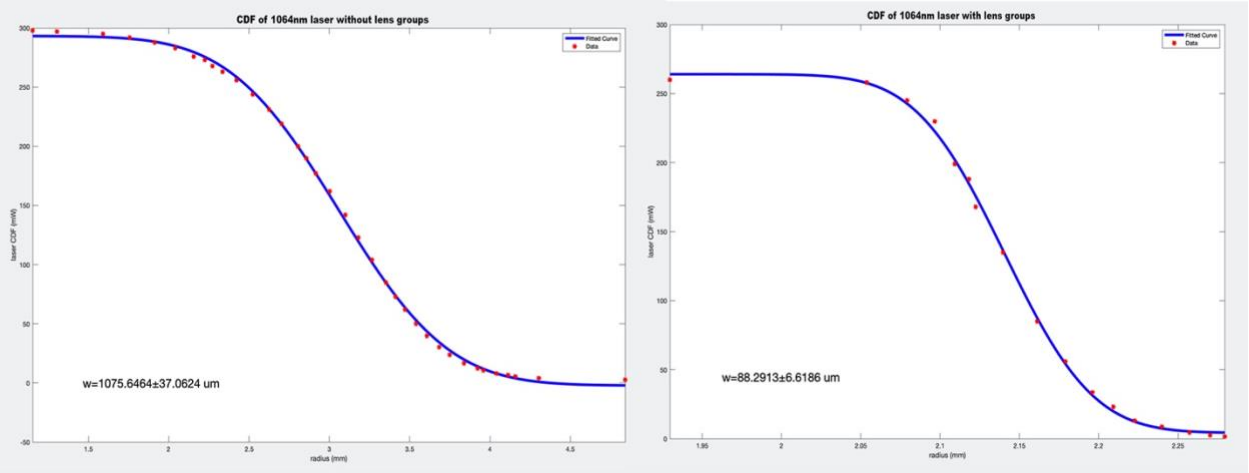

Figure 4.7. Fitting results for the beam width before (left) and after (right) beam-shrunk lens groups from knife-edge method.

4.6. Sample Specifications

El-Cat 2_9, an n-type (phosphorus-doped) monocrystalline silicon wafer is examined in this study. The wafer specifications are shown in Table 4.1. This wafer is FZ grown and double-side polished.

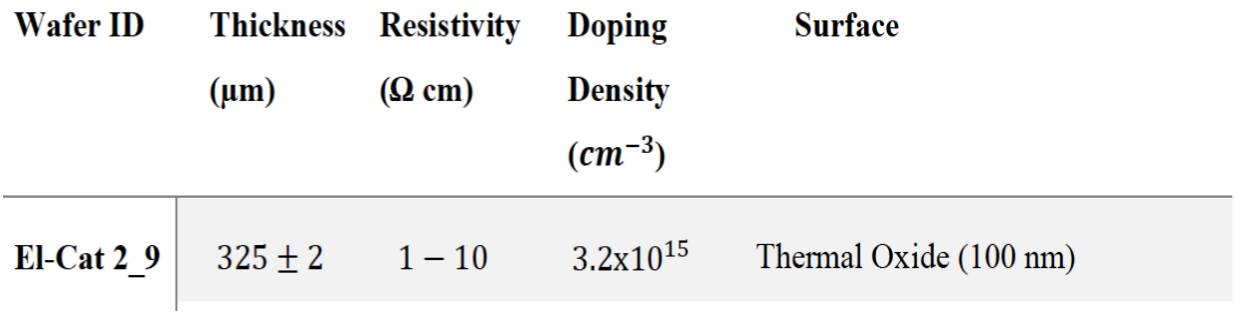

Wafer ID	**Thickness (μm)**	**Resistivity (Ω cm)**	**Doping Density (cm^{-3})**	**Surface**
El-Cat 2_9	325 ± 2	$1 - 10$	$3.2\text{x}10^{15}$	Thermal Oxide (100 nm)

Table 4.1. Specifications of Silicon Wafers Used in This Study.

5. Simulation Framework and Results

In this chapter, the simulation process consisting of computing integrated temperature, Lorentzian fitting for lifetime calculation, fixing resonance from EOM, smoothing data for diffusion distribution fitting, unwinding the phase and phase slope fitting, as well as diffusion distribution fitting will be discussed and the results from them will also be displayed and compared to the theory we discussed in chapter 4. Except the diffusion distribution fitting program which is written in Python programming language, all the other simulations are completed in MATLAB, and all the programs are written by myself. In the following parts of this chapter, I'll introduce them step by step.

5.1. Lifetime Extraction

After the experiment process that is discussed in chapter 4, we obtain the 640 by 512 temperature data of diffusion distribution at each frequency. The Lorentzian fitting requires the integrated temperature value for each frequency; before fitting the temperature value to Lorentzian curve, we need to compute the integrated temperature for each frequency. Given that we can't get rid of the background noise, which is random, in the temperature images, we need to come up with a method to skip its effect. We accomplish that by a method consisting of these steps: add all the values up, firstly and secondly, find the diffusion area by recording the point with the temperature value greater than the average temperature. We compared the average value for the whole image and the average exclude the diffusion area, the selection at one frequency is shown in Figure 5.1 and it can't influence the selection precision and our next steps.

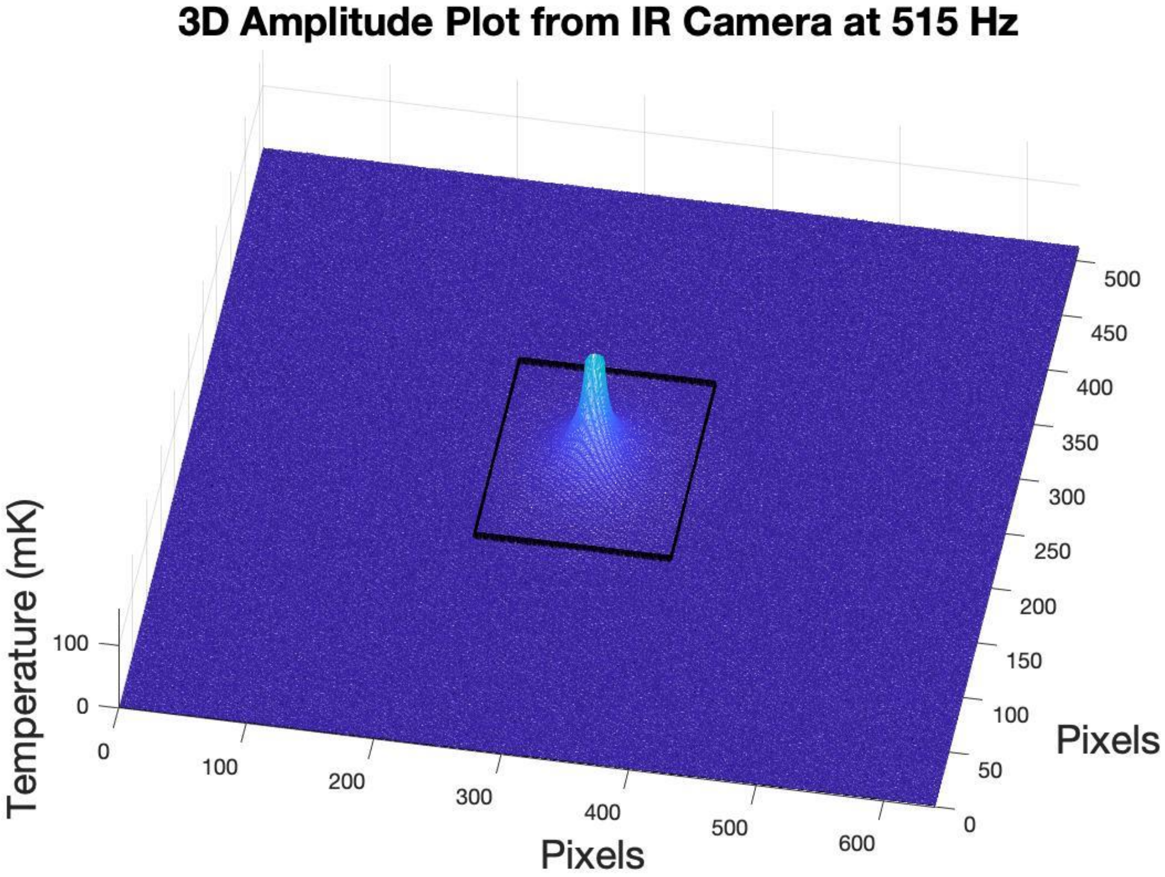

Figure 5.1. Background area selection. The area out of the black frame will be regarded as the background and used to compute the average background value.

Thirdly, we select four area from the background at the four corners of the image and compute the average value of them as the value of the background noise. We select as many background points as we can but we are careful about the boundary between the diffusion part and the background and set some buffer points which we ignore during the background value calculation. At last, we obtain the integrated temperature value by subtracting total background value from the total temperature value computed in step one.

After computing integrated temperature values for all the tested frequencies, we can fit them to the Lorentzian curve where we can obtain the fitted sample lifetime. The fitting program is written in

MATLAB, besides the fitted lifetime τ, another two coefficients are introduced to this fitting to make the experimental data match the theoretical one.

As was discussed in chapter 4, there can be resonance problem in pump and probe excitation. We measured the power of the pump and probe beam and compared them with the ratio computed by experimental amplitude over theoretical amplitude before and after resonance cancelling process. Because the bandwidth of the SR830 lock-in amplifier is limited at 100 kHz, data at frequency range between 100 kHz to 200 kHz is ignored. Given that high frequencies don't have resonance problem, we can use same resonance correction factor of 100 kHz as that of 100 kHz to 200 kHz. The experimental amplitude data is from smoothed data from camera after background noises cancelling and the smoothing process is discussed in the following part in this chapter. The theoretical data is calculated by the FCA model with the parameters calculated by carrier radial distribution analysis. The ratio is the average of the ratios at all the points. The normalized standard deviation is around 0.1 so we can use the average as the ratio at each frequency. The normalized plot is shown in Figure 5.2, where the pump intensity is shown in blue curve, the probe intensity is shown in green curve and the ratio before and after resonance cancelling are shown in black and cyan lines respectively.

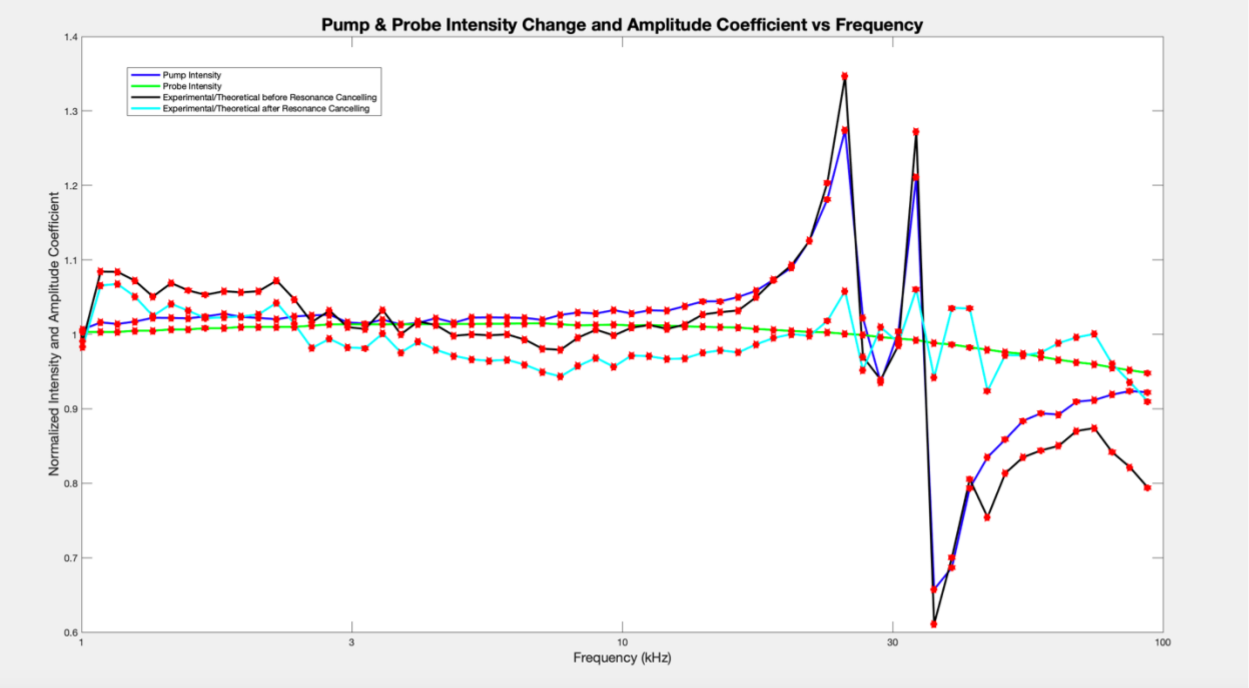

Figure 5.2. Normalized pump and probe intensity and ratio of experimental/theoretical amplitude value at all tested frequencies.

From Figure 5.2, we know that there is a problem caused by the resonance in pump beam which can influence the data measured by the camera. The probe beam has a relatively great stability and has almost no contribute on the camera data. Given that the resonance from EOM can influence the received power, in other words, the integrated temperature at each frequency, thus impacting the fitted lifetime calculation, we need to correct for it. Figure 5.3 shows the Lorentzian fitting with the data before the resonance cancelling and it is clear that there are some anomalous values that don’t match the curve at the range between 25 kHz to 40 kHz.

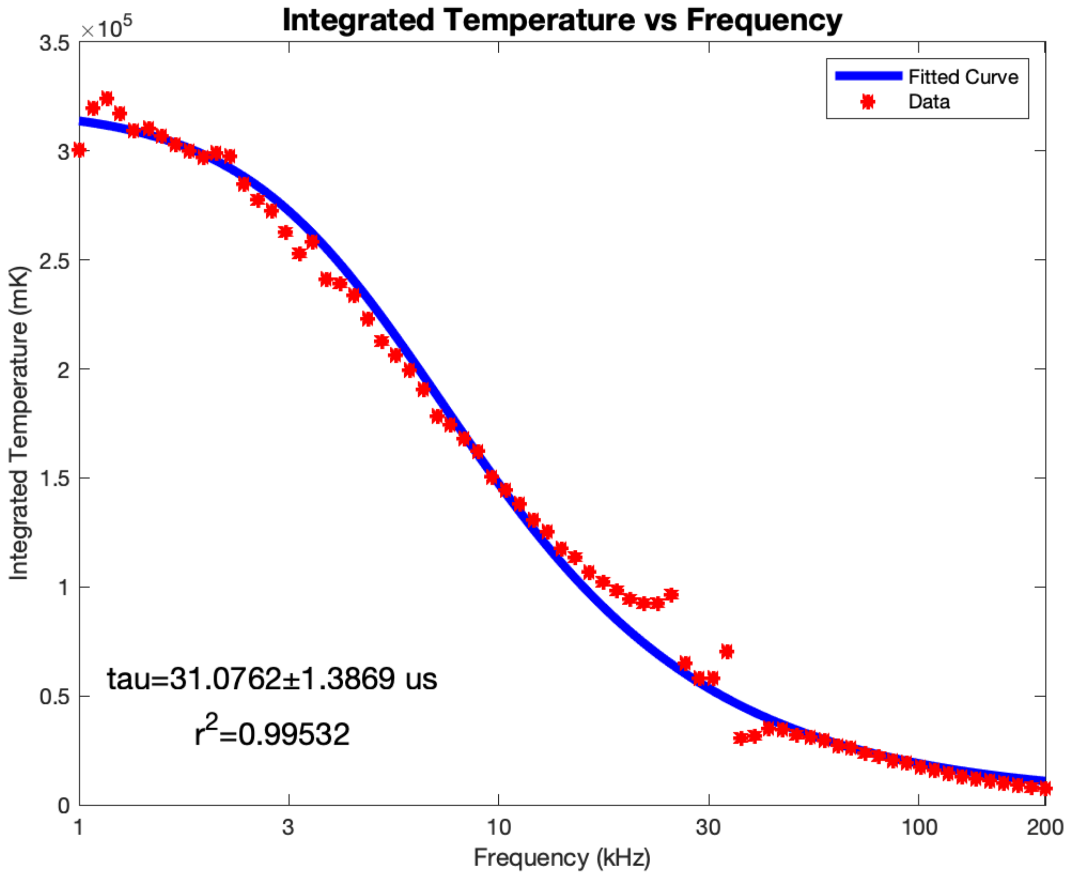

Figure 5.3. Lorentzian fitting with data before resonance cancelling.

Therefore, another MATLAB program correcting the resonance by dividing the normalized power from the resonance measurement branch at each frequency is used to modify the temperature value before Lorentzian fitting. Figure 5.4 shows the fitting result with data after the resonance cancelling. As we can see from Figure 5.3 and Figure 5.4, resonance cancelling mostly eliminates the anomalous range at 25 kHz to 40 kHz and the fitted lifetime is changed from 31.1 μs to 33.5 μs, which is closer to the extracted lifetime from carrier radial distribution analysis showing in the following part. From what has been discussed, resonance cancelling is important to the precision of this work, so all the values used in the final diffusion distribution fitting, including amplitude and phase data, will all be fixed by the resonance cancelling program before being used in the fitting calculation program.

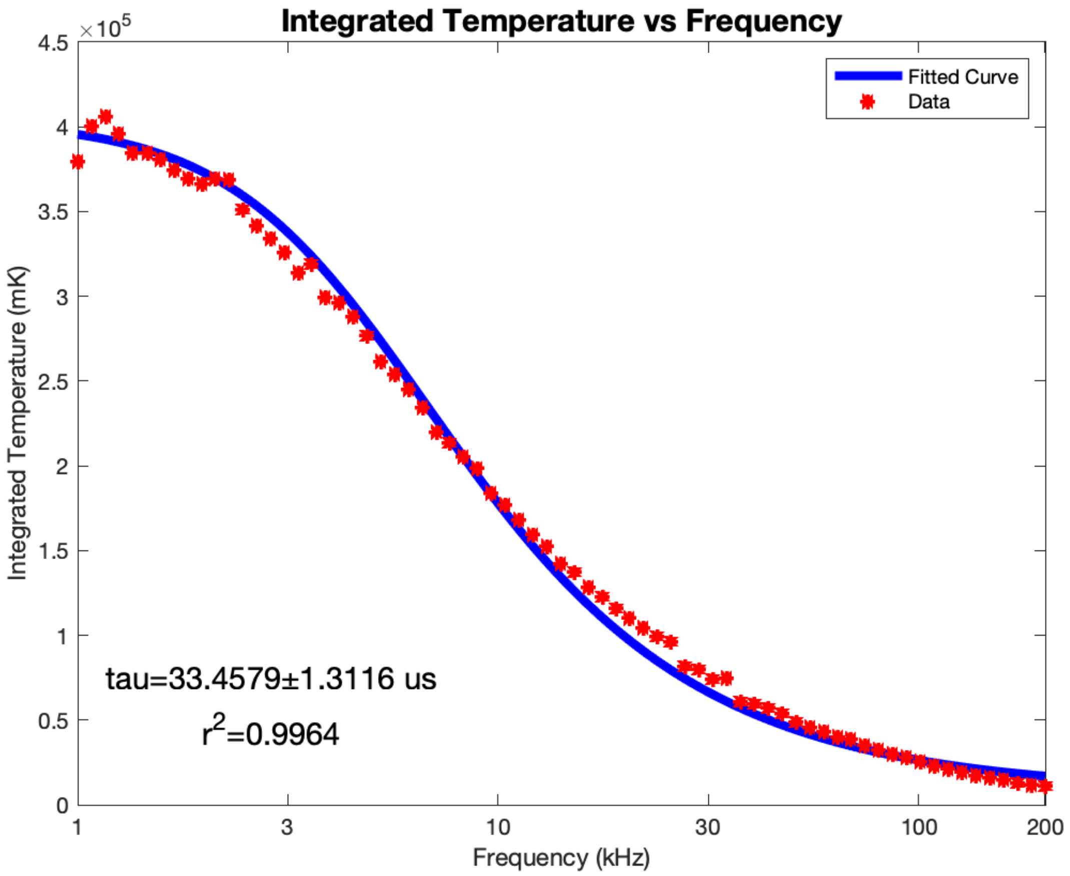

Figure 5.4. Lorentzian fitting with data after resonance cancelling.

5.2. Amplitude Analysis

Integrated temperature can be used in the Lorentzian fitting to obtain the fitted lifetime, the temperature curve, in other words, the amplitude of the diffusion distribution at each frequency can be used in the diffusion distribution fitting to obtain the fitted lifetime and diffusion coefficient simultaneously.

Different from Lorentzian fitting, which only needs the integrated value of each plot, the diffusion distribution fitting requires the whole plot to compute, thus we need to take the impact of the background noises more seriously. The data smoothing program is written in MATLAB to get rid of the impact from background noises. In the diffusion distribution fitting, only a one-dimensional curve from the center (the point with the max temperature) to the pixel is needed, which can be influenced to a great degree by the random noises. The basic idea of this program is to use the whole data from every single point to compute a smooth curve. The method is discussed here. The first step is to locate the center, which should be the point of max temperature. However, it can be not correct when we only take one point into consideration due to the random noises. Therefore, we sum all the values for each row and column up and find the max among the sums of rows and columns respectively. The cross point is used as the center point. For example, in this 640 by 512 image, if the row 328 has the max sum value among those of rows and column 257 has the max sum value among those of columns, the point (328,257) is marked as the center. When the center is located, we can transfer the image into a distance-based image. We mark every point with the distance to the center. Still using point (328,257) as an example, if the center point is located at (328,257), points at (328,256), (328,258), (327,257) and (329,257) all have distance 1 and points at (327,256), (327,258), (329,256) and (329,258) are all √2 away from the center. After marking the whole image by distance to center, we compute the average temperature value of the points with the same distance and finally, we are able to plot a one-dimensional smoothed curve from center to the pixel, which can be used in the diffusion distribution fitting. The comparison between the smoothed curve and one slide from the raw data is shown in Figure 5.5.

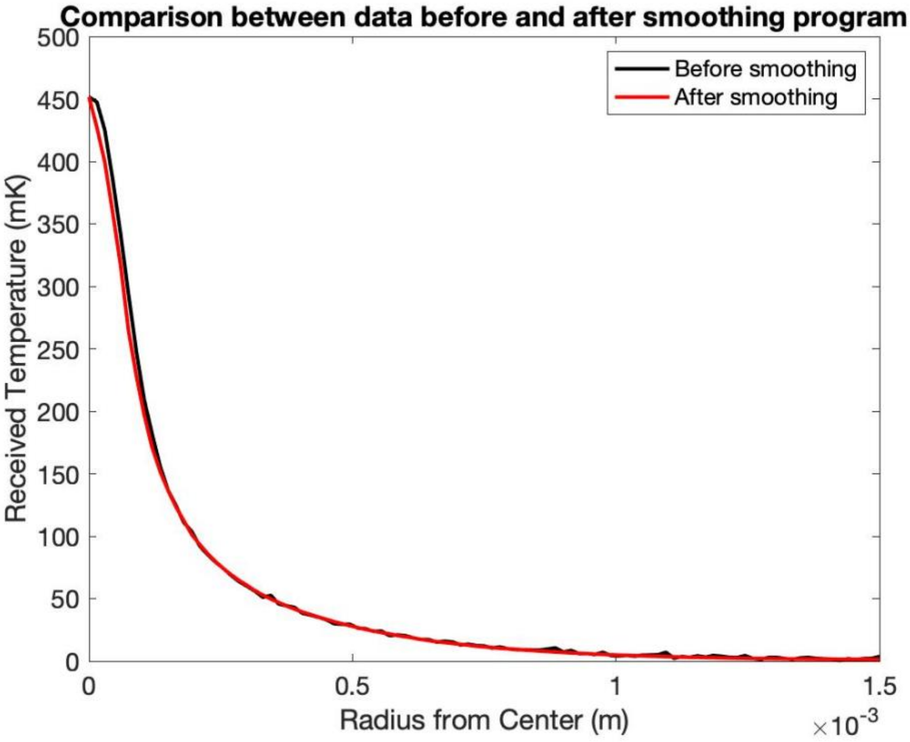

Figure 5.5. Comparison between amplitude data before and after smoothing program.

As we can see from Figure 5.5, data after smoothing can ignore almost all the influence from the background noises, which can be used in the amplitude analysis to compute τ and D.

The idea of the diffusion distribution fitting program written in Python can be clarified as follows. Given that the data from the camera is already in frequency domain and the formula of the carrier distribution is in time domain, the program needs to convert the carrier distribution formula into a frequency-dependent formula by Fourier Transform before the fitting process. Due to the precision of the knife-edge method, which is mainly used to test the utility of beam reducing system, the beam radius w can also be a variable in the fitting calculation. Besides that, we still need to introduce another two variables, amplitude coefficient a and background coefficient b into the fitting formula to make the value from the formula match that we obtain from camera. However, if we fit all these variables simultaneously, we can't obtain the reasonable results, 16 cm_2/s for D and 33 μs for tau. Besides, because more variables can have more freedom, the error bar of the fitted value is also beyond the tolerance. The fitting result for one frequency is shown in Figure 5.6.

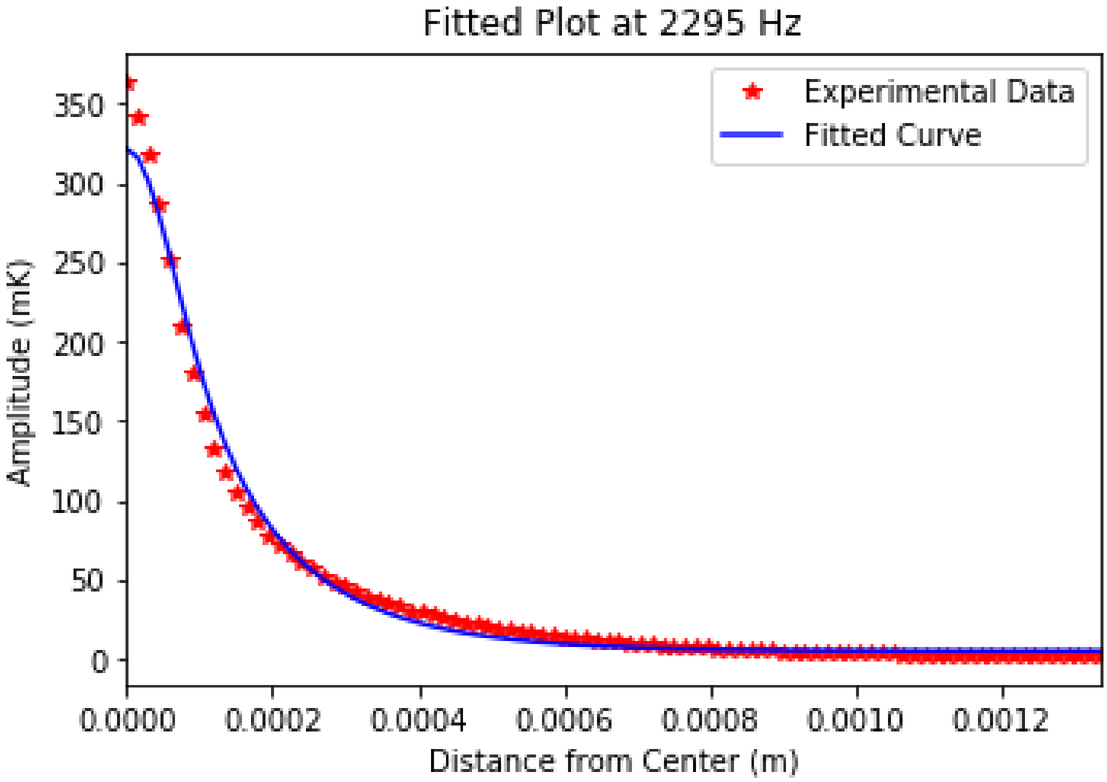

D = 10.000 ± 527.059 cm^2/s
w = 92.521 ± 144.407 um
tau = 32.489 ± 1906.404 us

Figure 5.6. Amplitude Fitting for D, w and τ at 2295 Hz.

Given that we have obtained the lifetime value from Lorentzian fitting, which is reliable, we fit the amplitude again by fixing tau at the value from Lorentzian fitting and computing D and w simultaneously. From this method, we can obtain the relatively reasonable results for every frequency but there is still a difference on beam radius between the fitted one and the one from knife-edge. In Figure 5.7, we present fitting results for several frequencies in the tested frequency range.

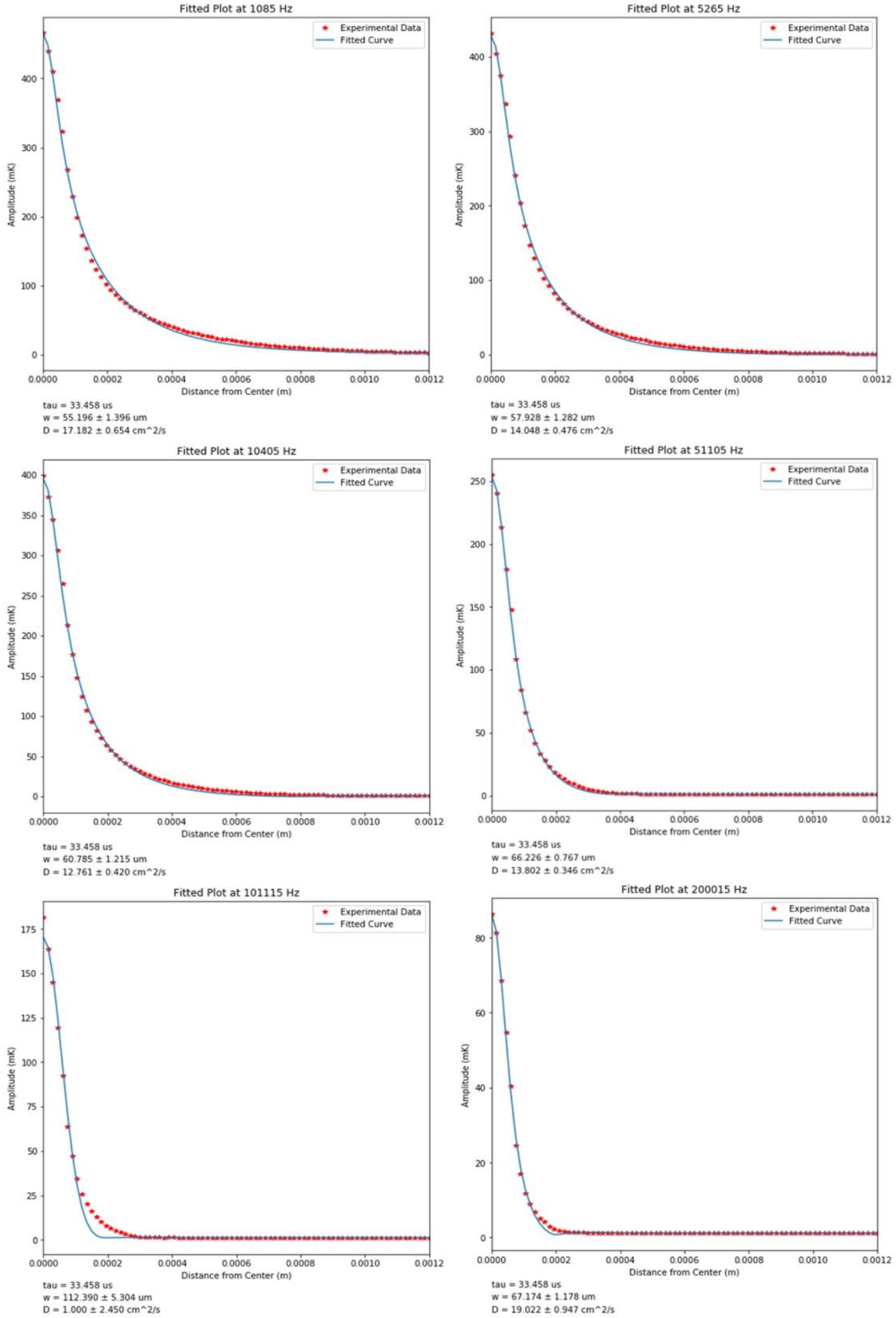

Fitted Plot at 1085 Hz

tau = 33.458 us
w = 55.196 ± 1.396 um
D = 17.182 ± 0.654 cm^2/s

Fitted Plot at 5265 Hz

tau = 33.458 us
w = 57.928 ± 1.282 um
D = 14.048 ± 0.476 cm^2/s

Fitted Plot at 10405 Hz

tau = 33.458 us
w = 60.785 ± 1.215 um
D = 12.761 ± 0.420 cm^2/s

Fitted Plot at 51105 Hz

tau = 33.458 us
w = 66.226 ± 0.767 um
D = 13.802 ± 0.346 cm^2/s

Fitted Plot at 101115 Hz

tau = 33.458 us
w = 112.390 ± 5.304 um
D = 1.000 ± 2.450 cm^2/s

Fitted Plot at 200015 Hz

tau = 33.458 us
w = 67.174 ± 1.178 um
D = 19.022 ± 0.947 cm^2/s

Figure 5.7. Amplitude fitting with fixed τ at several frequencies in the tested range from 1 kHz to 200 kHz.

From these fittings, the results are better but still can be further improved. The fitted beam size w varies from 55 μm to 73 μm and fitted D varies from 12 cm$_2$/s to 19 cm$_2$/s. Besides that, some problem happens at some point of high frequencies, which failed to return reasonable values. The aim of this work is to compute τ and D simultaneously. We can do this with the fixed beam width. However, the fitted w varies from frequency to frequency and we can't compute the average from them. This issue can be interpreted that amplitude only gives us a half of the information and we need to take the phase data into account.

5.3. Phase Analysis

Before fitting the phase data, we need to understand the regular pattern of phase curve. We compute the real part and imaginary part of the carrier distribution formula to compute the phase. The experimental and theoretical phase vs. position curve is shown in Figure 5.8, from which we know that the phase follows a periodic linear function.

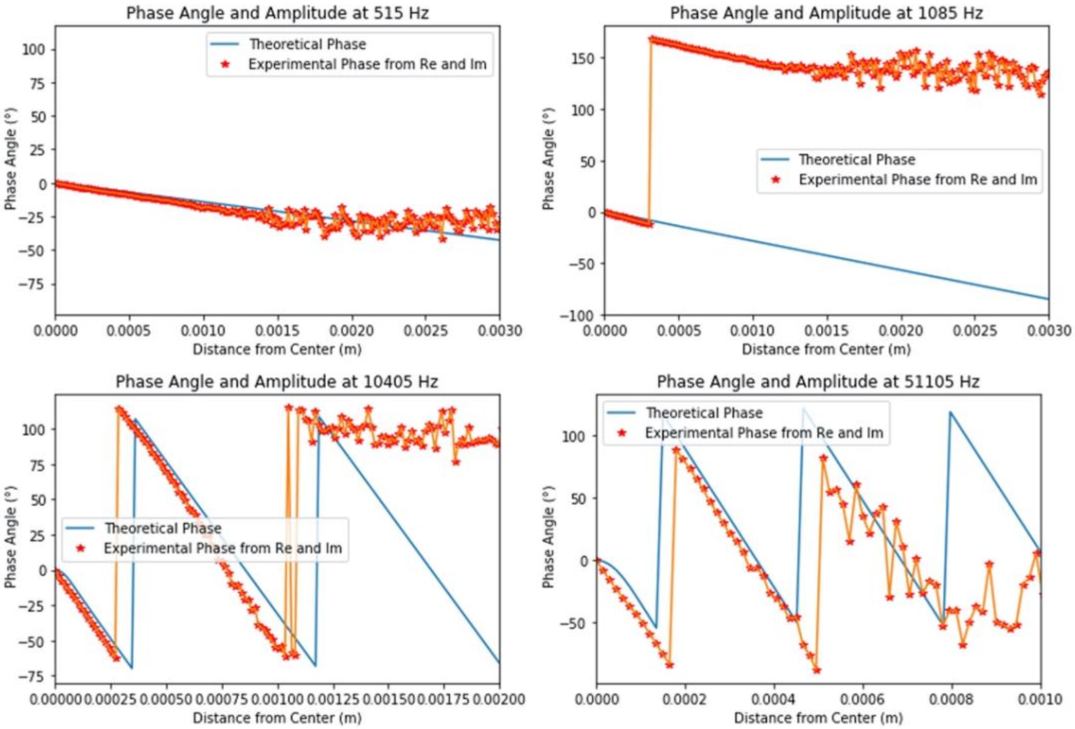

Figure 5.8. Phase from camera data and computed theoretically vs position.

The formula derivation discussed in chapter 4 confirms this point. Therefore, we only need to fit the phase slope and we can have all the information we need.

The phase data also needs to be smoothed and the method is same as that of amplitude smoothing process. We use the same point as the center as that of amplitude and same method to compute the average value to smooth the data. As what is shown in Figure 5.8, the phase curve is frequency-dependent periodic and can have a 2π gap at each period, we need to unwind the phase curve, which is done in MATLAB, to make it a straight line. Figure 5.9 shows the unwound phase from 1 kHz to 200 kHz in the whole image range and selected range, from which we can know that phase can be influenced badly by the background noises and the influenced range is depend on the diffusion range that varies by frequencies.

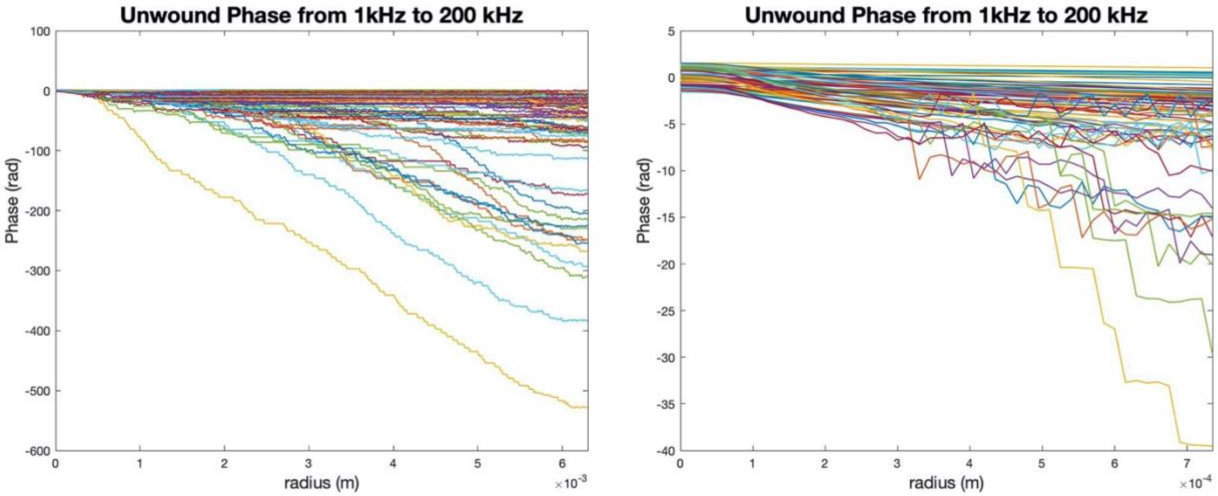

Figure 5.9. Unwound phase data from 1 kHz to 200 kHz in the whole image range (left) and selected range (right).

Therefore, the usable range of unwound phase data is different at different frequency. Taking that into account, we divide the tested frequency into three groups, 1 kHz to 10 kHz, 10 kHz to 70 kHz and 70 kHz to 200 kHz, which have different selected range to make the unwound phase data possible to be fitted as a linear function. Figure 5.10 shows the selected unwound phase data for all three frequency classes.

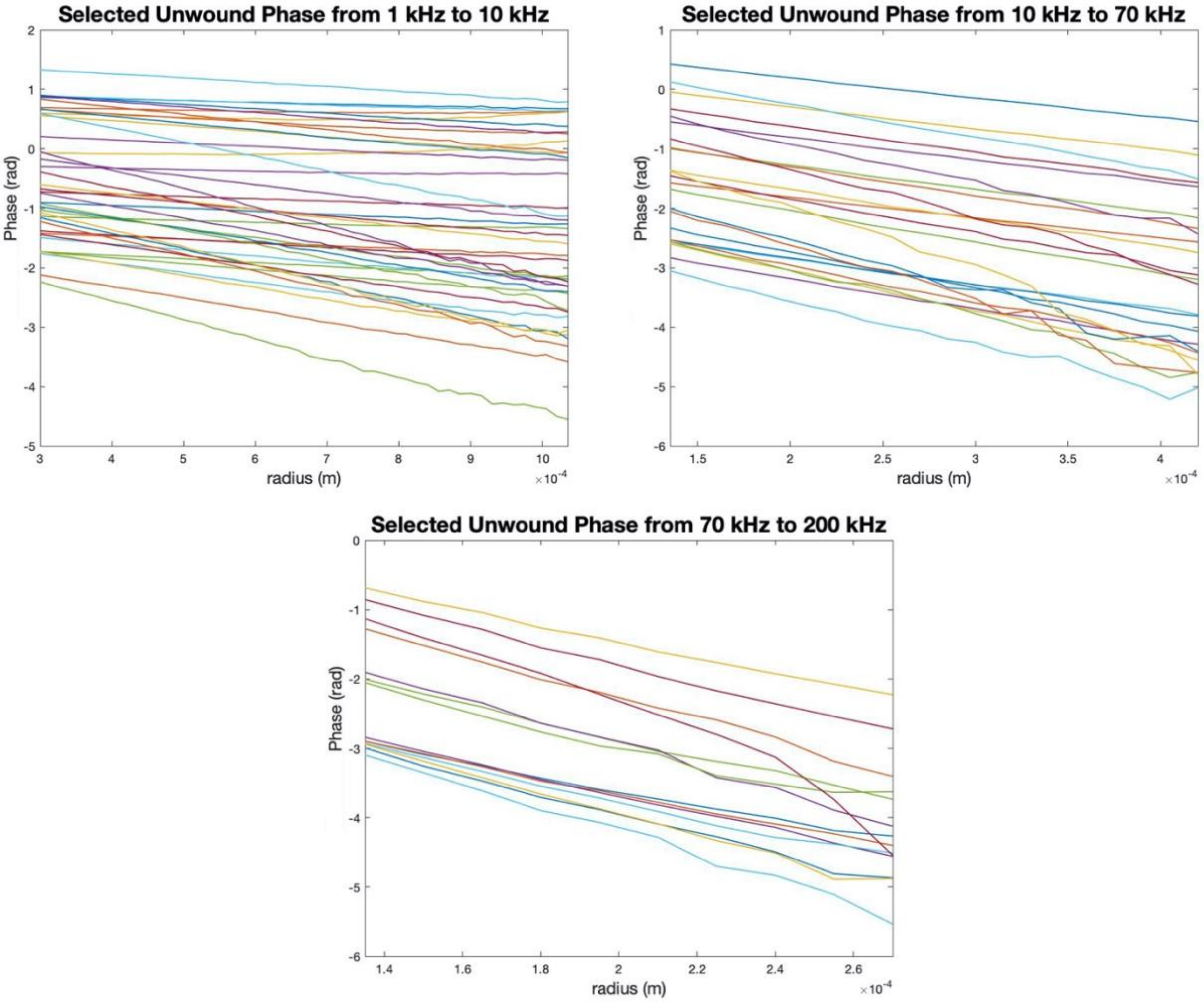

Figure 5.10. Selected unwound phase data for different frequency classes.

Then we can fit the phase slope for every frequency, as well as fit the slope for all the frequency we test. Equation 3.2.5 gives us the formula of the phase slope, and we can use it for the fitting between frequency and phase slope to substitute D and τ. Figure 5.11 shows the phase slope fitting result of several frequencies.

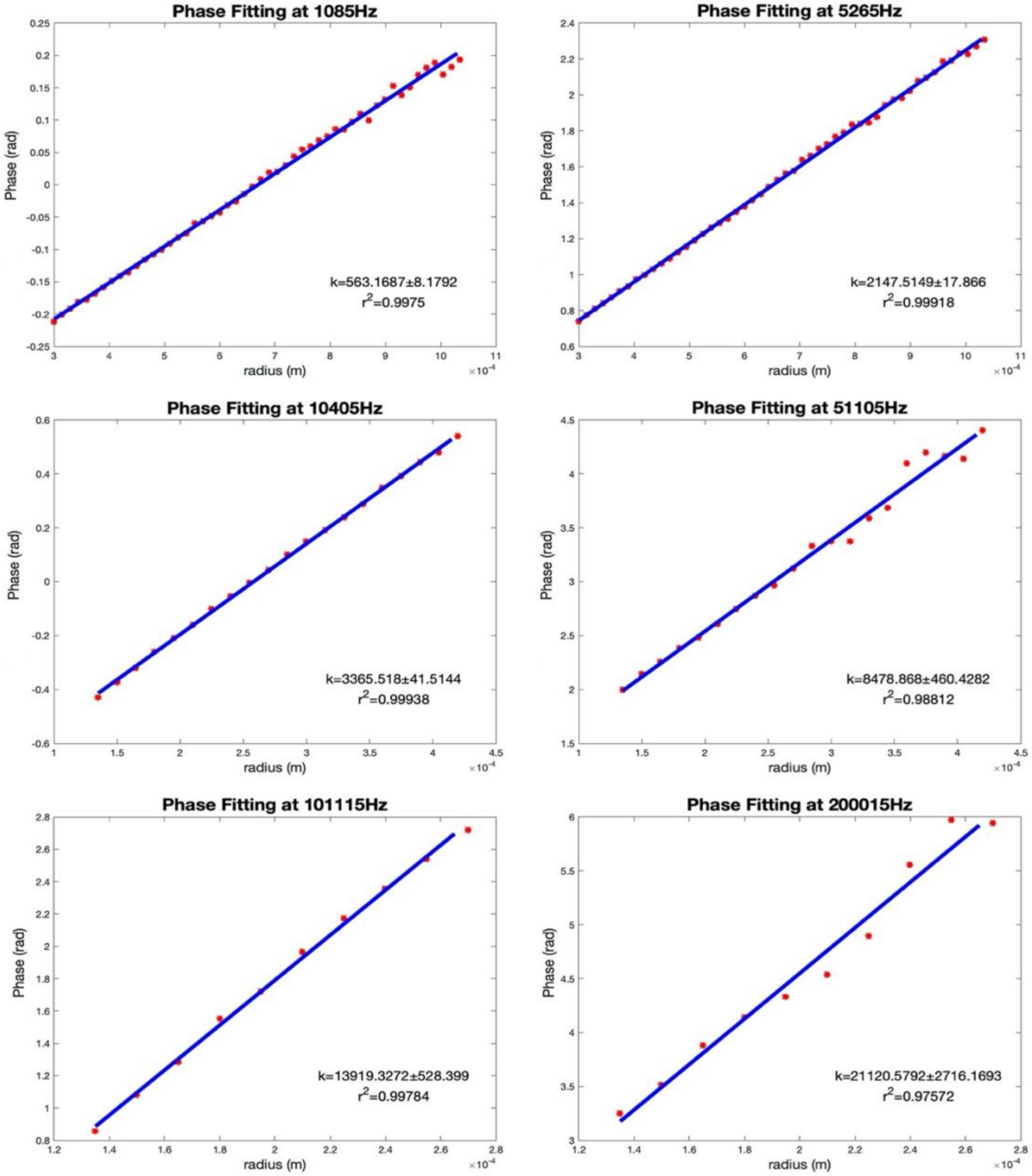

Figure 5.11. Phase slope fitting at several frequencies in the tested range from 1 kHz to 200 kHz.

From Equation 3.2.4, we can extract D and τ by the phase slope fitting for each frequency but the fitting result can be influenced by several factors and the data at one frequency is not enough to meet the precision requirement, which makes the fitted value unreliable. Therefore, we make the phase slope a function depending on frequency and fit all the slope. The fitting result is shown in Figure 5.12. As what has been discussed in chapter 3, there's an assumption during the formula derivation that the pump beam radius w_{pu} is smaller enough than the probe beam radius w_{pr}, the fitting doesn't match the theory when we use the data from the system without the beam shrinking lens groups. Therefore, that's another main reason for us to add these lens group in our experiment system to shrink the beam size. The phase slope fitting results before the beam shrinking is also shown in Figure 5.12.

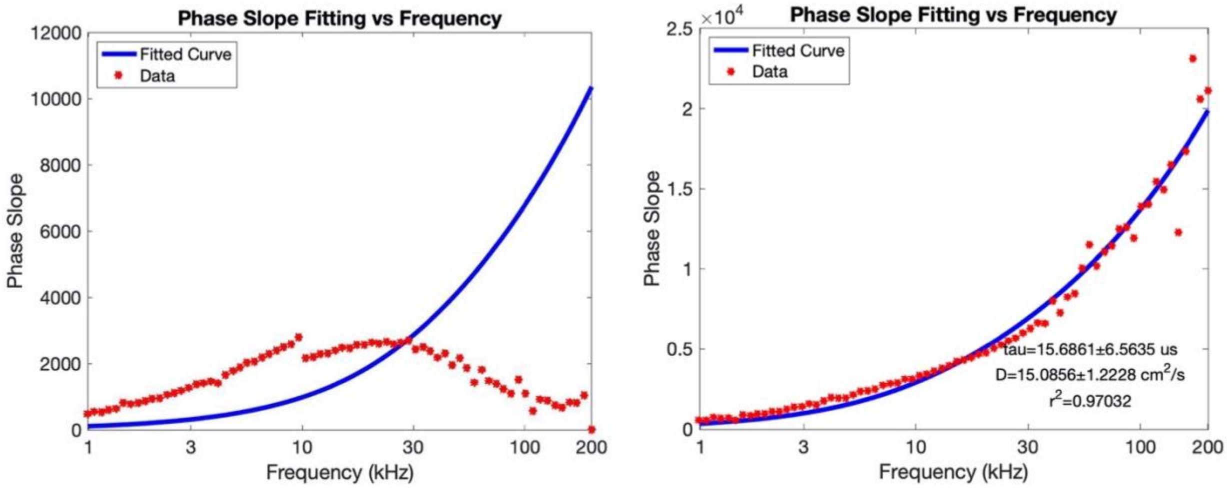

Figure 5.12. Phase slope fitting with frequency from the data before (left) and after (right) the beam shrinking lens groups. Because of the large beam size, the data plot from the beam without the lens groups can't match the theoretical curve.

However, even though the shape matches the fitting one with the shrunk beam and the fitted D is reasonable, we can't obtain the value of τ from this fitting process to match that from Lorentzian fitting. We suspect that it may be caused by the beginning of the phase shape. The phase of the points near the center doesn't follow linear function but a curve, which can't be fitted in this method. Unfortunately, we can't write the frequency-dependent carrier distribution formula into a closed format, we don't know the actual pattern of it, so we still need to get back to fit the phase from the carrier distribution formula. The method and result of the phase fitting in python are almost the same as these of amplitude fitting, the result from phase fitting with fixed τ from Lorentzian fitting is not as reasonable as that from amplitude fitting. Figure 5.13 shows plots of phase fitting at several frequency in the tested range.

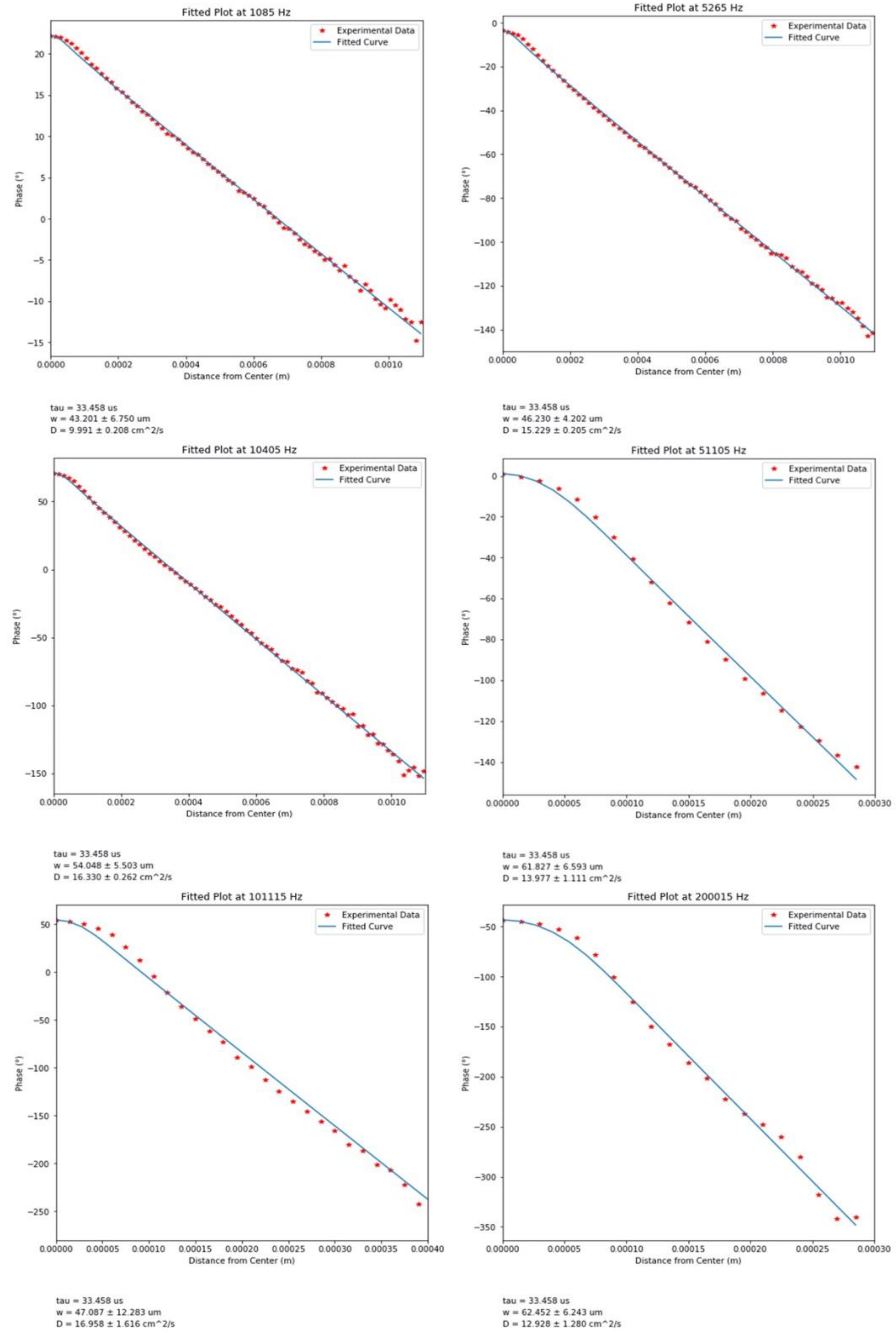

tau = 33.458 us
w = 43.201 ± 6.750 um
D = 9.991 ± 0.208 cm^2/s

tau = 33.458 us
w = 46.230 ± 4.202 um
D = 15.229 ± 0.205 cm^2/s

tau = 33.458 us
w = 54.048 ± 5.503 um
D = 16.330 ± 0.262 cm^2/s

tau = 33.458 us
w = 61.827 ± 6.593 um
D = 13.977 ± 1.111 cm^2/s

tau = 33.458 us
w = 47.087 ± 12.283 um
D = 16.958 ± 1.616 cm^2/s

tau = 33.458 us
w = 62.452 ± 6.243 um
D = 12.928 ± 1.280 cm^2/s

Figure 5.13. Phase fitting with fixed τ at several frequencies in the tested range from 1 kHz to 200 kHz.

The stability of fitted values from phase fitting is similar to that of values from amplitude fitting. The fitted D varies from 9 cm^2/s to 17 cm^2/s and fitted w varies from 43 μm to 62 μm. From what has been discussed before, we know that we can't make the full use of the experimental data when fitting amplitude or phase alone. In order to use the whole data to compute the lifetime and diffusion coefficient, we tried to fit the phase data and amplitude data simultaneously.

5.4. Carrier Radial Distribution Analysis

The idea of this phase-amplitude fitting is simple, which is to create an artificial piecewise function consisting of phase part when $r<0$ and amplitude part when $r>0$ and then we could generate a new piecewise function for fitting. It seems that we could run this fitting immediately but there's a point we shouldn't ignore, the relative weighting. Given that the value of amplitude (more than 300 mK for max at low frequencies and around 50 mK at high frequencies) is different as compared to that phase with a roughly 180 degrees range during the fitting area, which can make the weight for fitting different and not equal for each frequency, we compute the integrated phase value and amplitude value which are used to compute the balancing coefficient for these two parts for each fitting; therefore, the values showing in Figure 5.14, which shows the results from phase-amplitude fitting for D and w with fixed τ for several frequencies are not the real data but the equivalent after the calculation of the balancing coefficient.

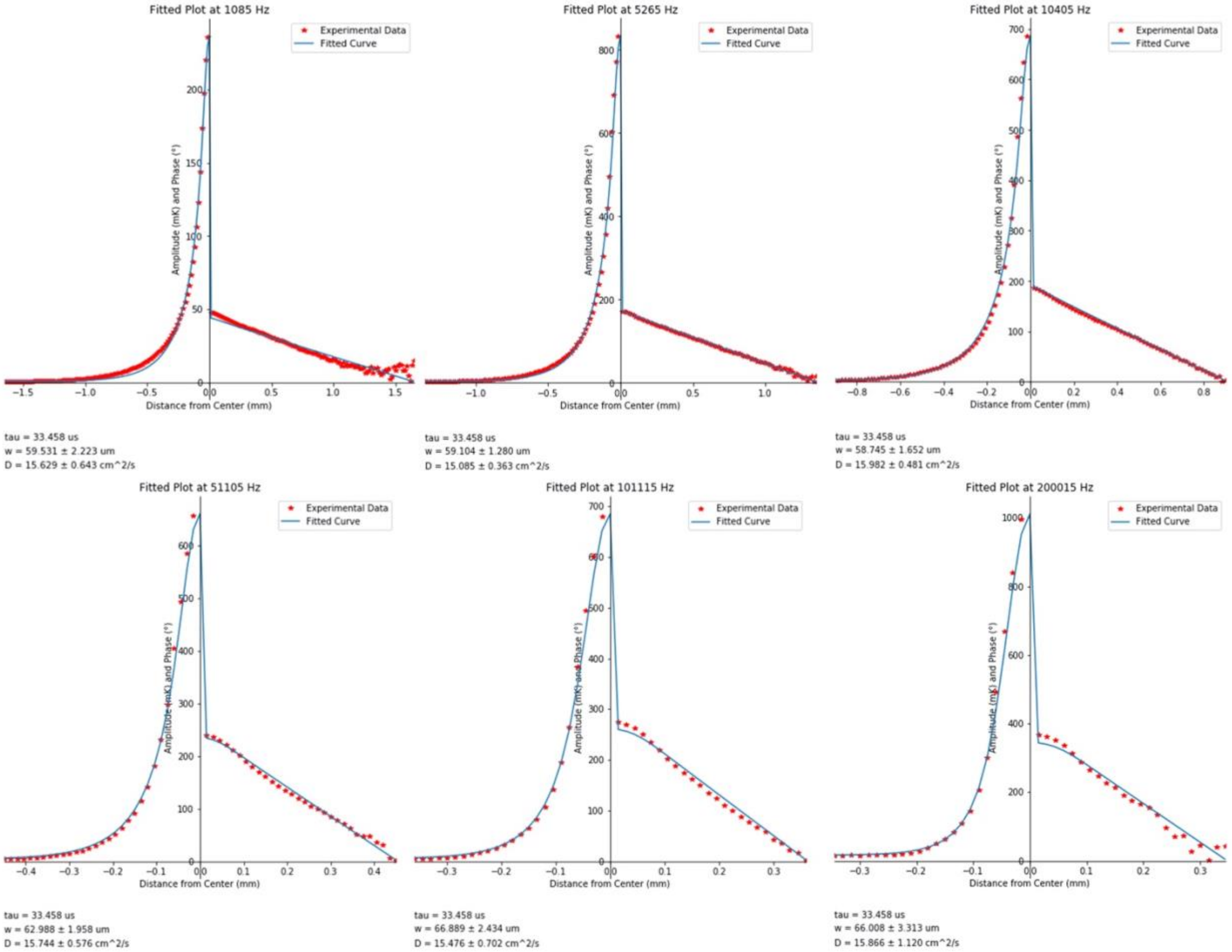

Figure 5.14. Carrier distribution fitting with fixed τ at tested frequencies from 1 kHz to 200 kHz.

From Figure 5.14, we can see that fitted ω and D are both reasonable and stable during the tested frequency range. In order to evaluate the stability of the fitted value, we make a summary for fitted D and w which is shown in Figure 5.15, and the normalized summary can be found in Figure 5.16.

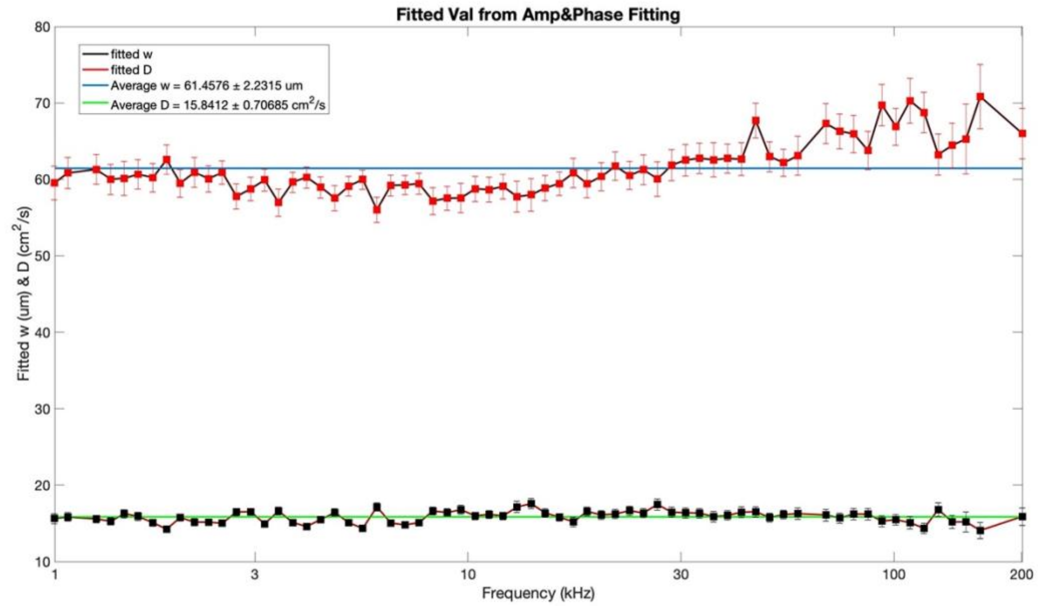

Figure 5.15. Summary of the fitted D and w.

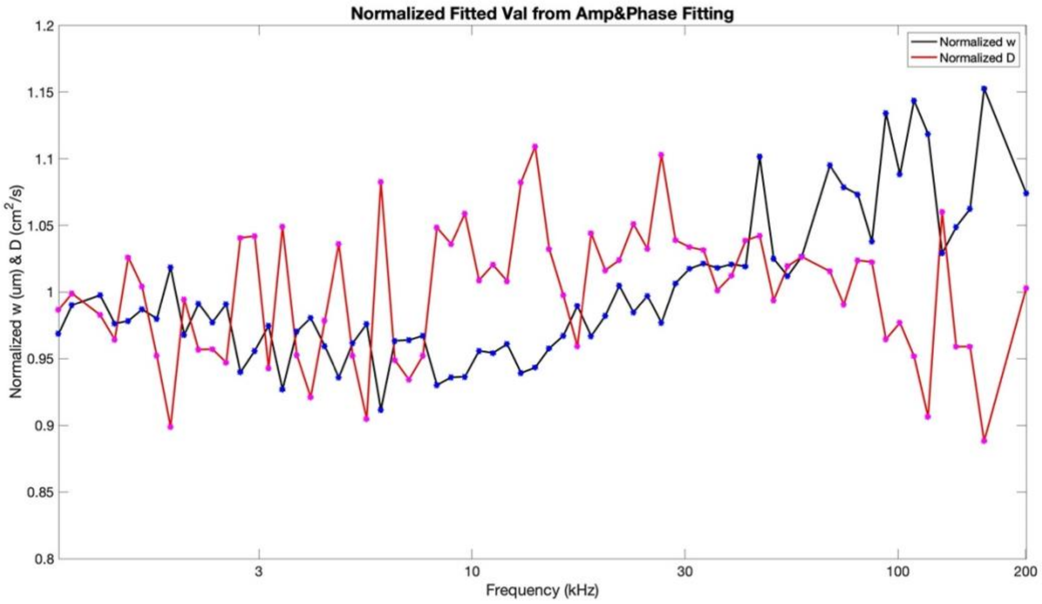

Figure 5.16. Summary of normalized fitted D and w.

The average fitted D is 15.8 ± 0.7 cm$_2$/s, which matches the theory well and the average fitted beam size w is 61.5 ± 2.2 μm, which has some difference to that measured by the knife-edge method, 88.3 μm. However, the reason for us to use knife-edge method to measure the beam size is to see the effect of the beam shrinking system and the precision of it is not enough to make it a reference of the true value of beam size. In the experiment, we can’t make the knife perfectly vertical to the beam and the power meter used in this process fails to provide the enough precision either. Therefore, we prefer to use this fitted beam size as the initial input parameter in our final fitting to extract D and τ, which gives us a reasonable and good result showing in the following part. It will be better if we can have another precise method to measure the beam size to verify our theory and it can be one of the future work. As what have been discussed above, the fitted values are stable and we can use the average beam radius for the fitting to compute D and tau together. Before doing the fitting of D and τ, we compared the amplitude and phase curve with the average D and w and that with the fitted D and w at each frequency. Figure 5.17 shows several plots for this comparison and the two plots at each image coincide very well.

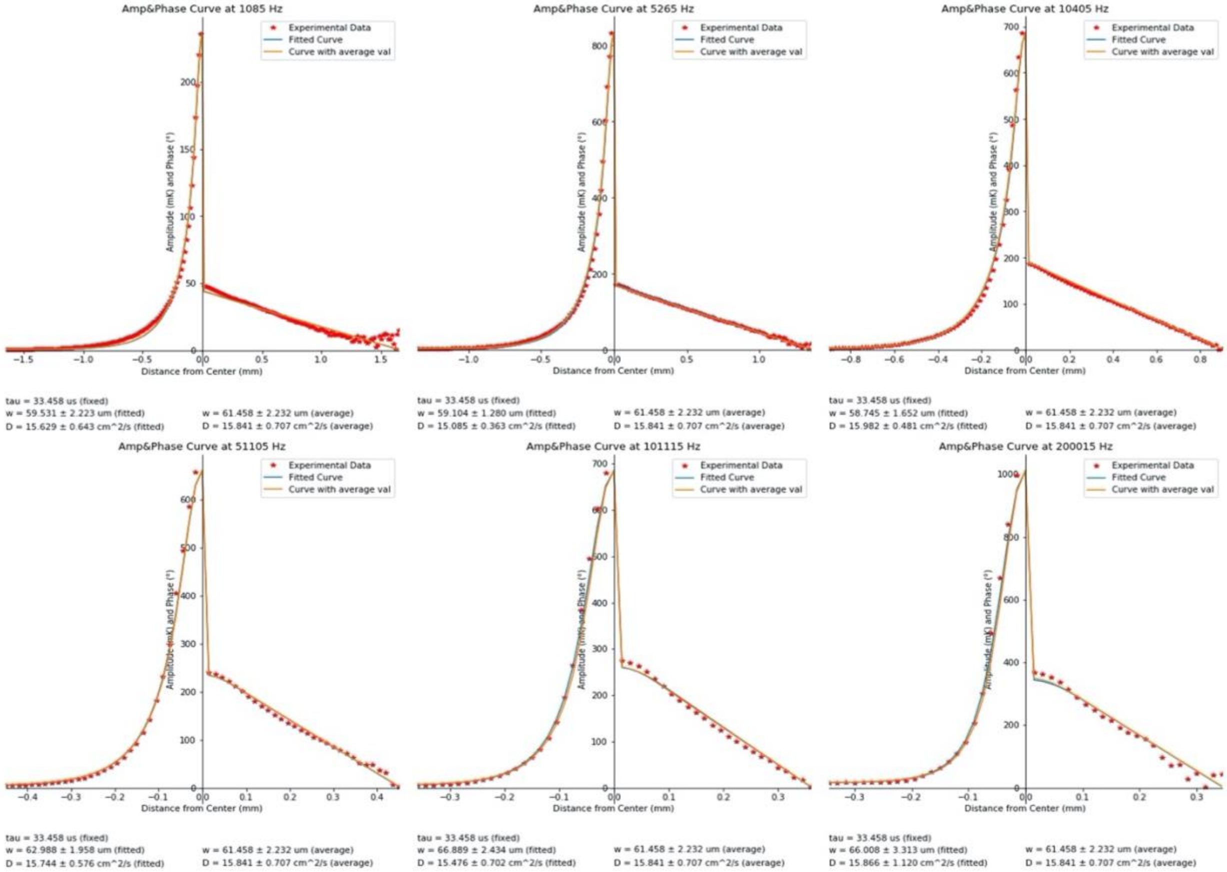

Figure 5.17. Comparison between curves with fitted value (blue) and average value (orange). The two curves coincide very well.

Then we can fix the beam width w and fit lifetime τ and diffusion coefficient D simultaneously. Figure 5.18 shows the several fitting results for the calculation of D and τ and Figure 5.19 shows the summary of the final fitting. The normalized summary of fitted D and τ is shown in Figure 5.20. From these images, we can obtain a reasonable value for D, which fit that from theory of 16 cm$_2$/s and τ, which match the value computed by the Lorentzian fitting.

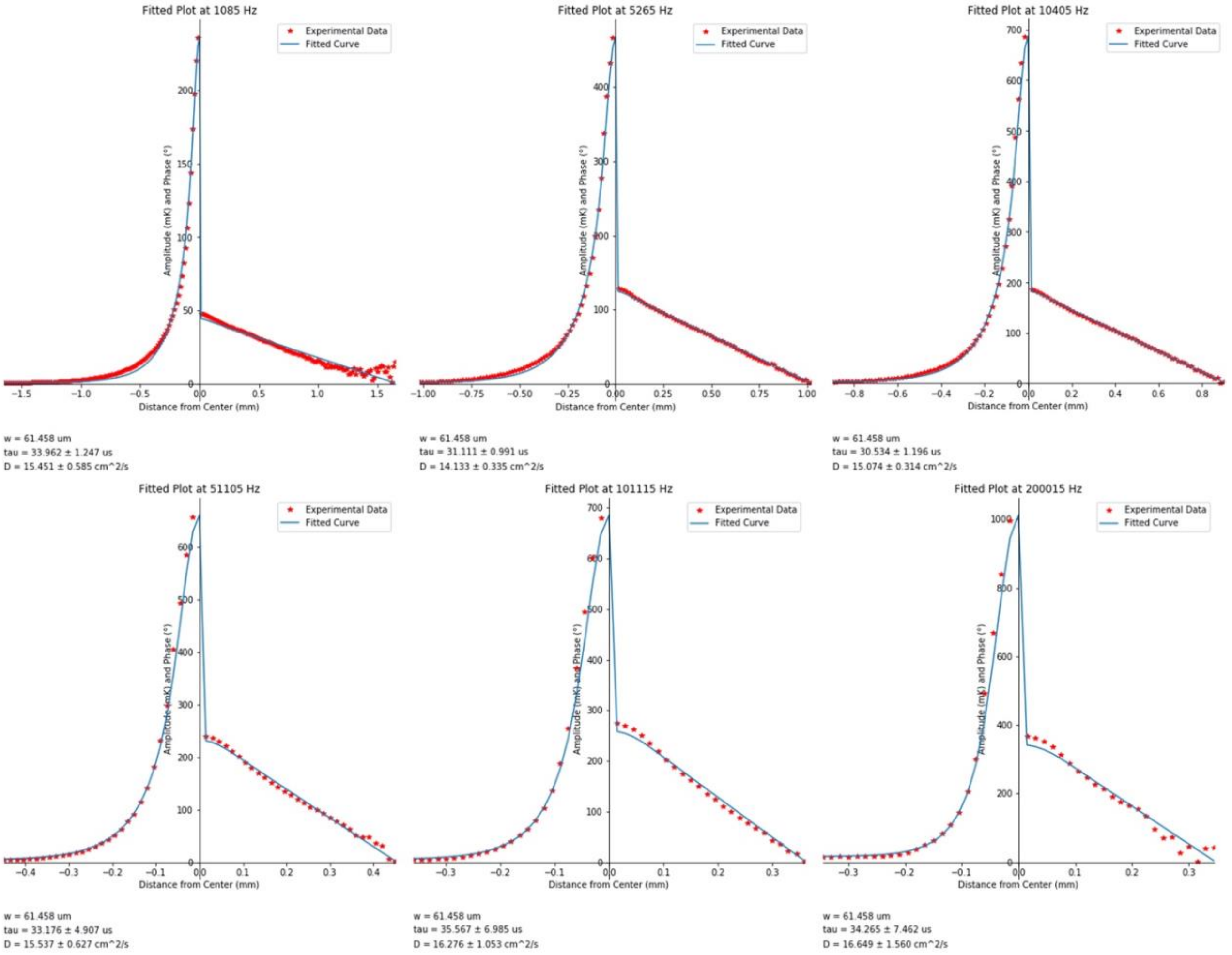

Figure 5.18. Carrier distribution fitting with fixed ω at tested frequencies from 1 kHz to 200 kHz.

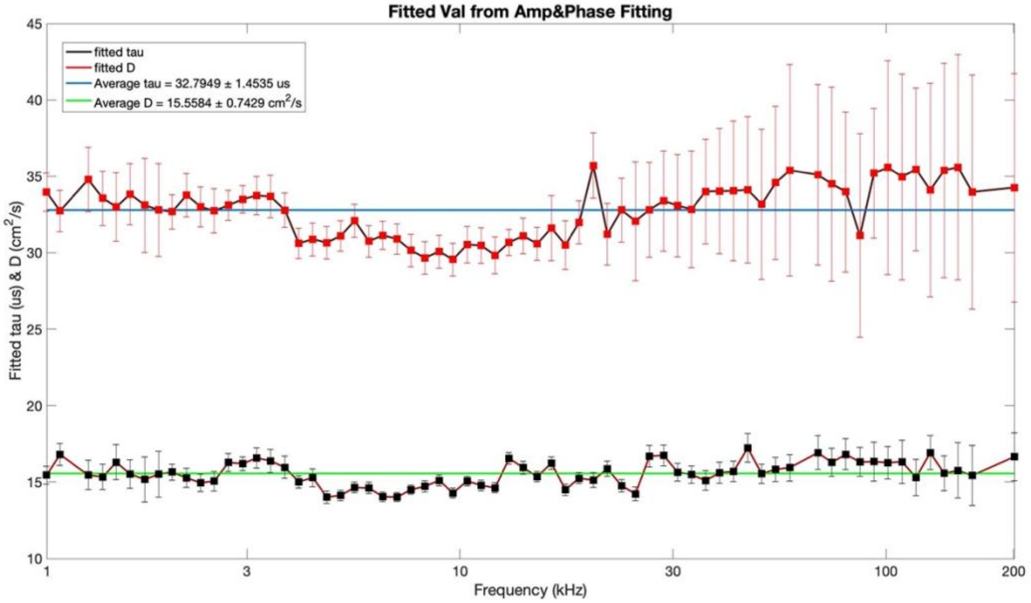

Figure 5.19. Summary of the fitted D and τ.

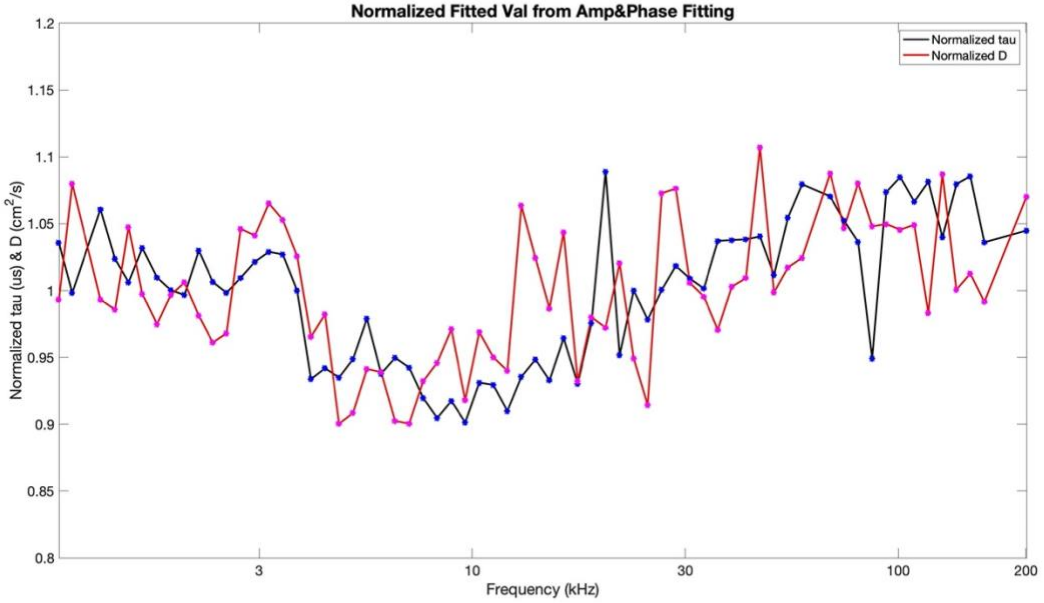

Figure 5.20. Summary of normalized fitted D and τ.

The average fitted lifetime τ = 32.8 ± 1.5 μs and the average fitted diffusion coefficient D = 15.6 ± 0.7 cm$_2$/s, which show that the theory is suitable for all the tested frequencies. Then we did the same comparison between the curves with fitted D and τ and these with average D and τ, they match very well and the comparison can be found in Figure 5.21.

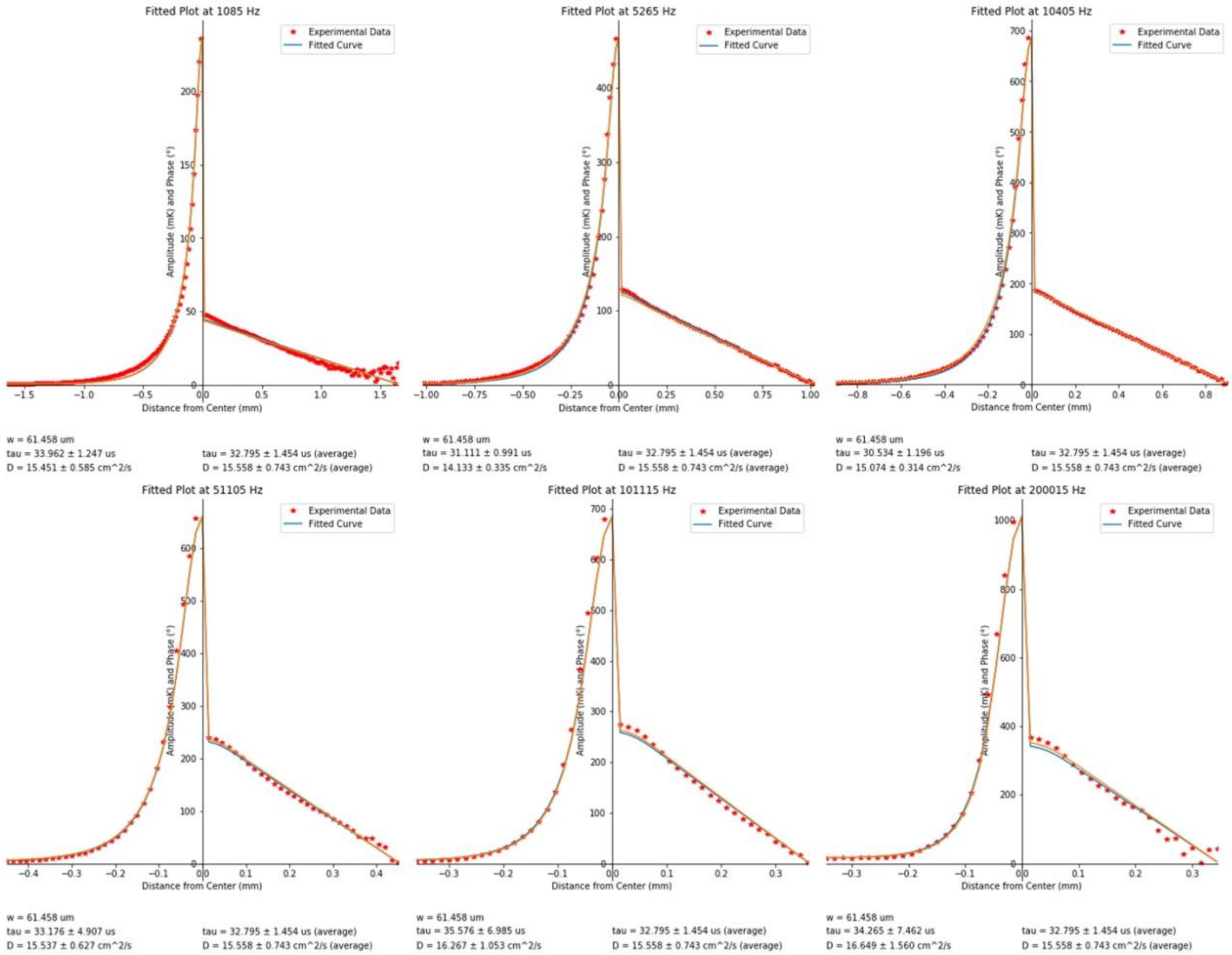

Figure 5.21. Comparison between curves with fitted value (blue) and average value (orange). The two curves coincide very well.

6. Conclusion and Future Work

6.1. Conclusion

In this dissertation I reviewed a new and improved technique for the measurement of recombination lifetime and diffusion coefficient in semiconductors, particularly suitable for silicon, developed by Dr. Kevin M.W. Boyd, and I did an experiment based on this method and finished the simulation process, from which we can obtain results with good quantitative agreement to theory that confirm the feasibility of this method.

In this experiment, the pump is a 1064 nm single mode laser beam with beam width at around 60 μm, which is much smaller than that of the probe LED. The LED generates a 2050 nm radiation that is uniform in the tested area of the wafer, which can meet the assumption in the equation derivation.

In this experiment we apply the measurement at a frequency range from 1 kHz to 200 kHz and analyze every single data at each frequency. The results are stable and reliable. The fitted lifetime from this 3D FCA model is 32.8 ± 1.5 μs, which matches that from frequency-domain free-carrier concentration equation (33.5 ± 1.3 μs) very well within the error bars. The fitted diffusion coefficient from this 3D FCA model is 15.6 ± 0.7 cm^2/s, matching the theoretical value which should be 16 cm^2/s for silicon. From what has been tested, this 3D FCA model has the ability to extract lifetime and diffusion coefficient simultaneously. Besides that, this model is fully general, accounting for the 3D transport of free-carriers in a semiconductor, as well as recombination in the bulk and at the surface. Furthermore, because the equation was solved for a Gaussian-shaped excitation it is applicable to any experiment employing single-mode lasers.

6.2. Future work

There is some necessary work to be done in the future in order to improve the precision of the experiment and the simulation process. In the experiment part, it will be better if we could measure the wafer lifetime in other ways to verify the value we obtain from Lorentzian fitting or FCA fitting, though they match each other well. We tried to measure it with MDP map from Freiberg Instrument but the result isn’t reliable because we can’t match the settings of injection level, pump radiation intensity and wavelength to that of our experimental settings. Another work to improve this experiment is to measure the beam width precisely. The result from knife-edge is not precise enough, which has some difference from the fitted value. It can be a good supplementary proof of our theory.

In the simulation process, we only fit the measured data to the FCA model at each frequency at one time. Even though the fitted values show good stability with frequency and we can trust the fitting results, it will be better if we can find some way to fit all the data at all the test frequency simultaneously, which can give us more precise result than the average value. It’s not simple because for one thing, the diffusion spot can shrink with higher frequency, which causes that the quantity of usable data point are different from frequency to frequency; for another, because of the difference of usable data point, it can be difficult to define the balance weight coefficient for each frequency, for the initial center value at different frequency is different. If we could find some method to overcome these problems and fit all the data simultaneously, we can obtain an overall fitted lifetime and diffusion coefficient, which can be more precise and reliable.

References

[1] Renewables 2020: Global Status Report, Ren21. 2020. p. 107.

[2] International Energy Agency — Photovoltaic Power Systems Programme. 30 March 2015.

[3] Photovoltaic Effect Archived 14 July 2011 at the Wayback Machine. Mrsolar.com. Retrieved 12 December 2010.

[4] The photovoltaic effect Archived 12 October 2010 at the Wayback Machine, Encyclobeamia.solarbotics.net, Retrieved on 12 December 2010.

[5] https://commons.wikimedia.org/wiki/File:Solargif1.gif.

[6] S. Rühle, "Tabulated values of the Shockley–Queisser limit for single junction solar cells," Solar Energy., 2016, 130: 139–147.

[7] Vos, A. D, "Detailed balance limit of the efficiency of tandem solar cells," Journal of Physics D: Applied Physics., 13 (5): 839.

[8] https://commons.wikimedia.org/wiki/File:ShockleyQueisserFullCurve.svg.

[9] https://www.pveducation.org/pvcdrom/pn-junctions/absorption-coefficient.

[10] Kñfferlein, M., T. Dñhring, H.D. Payer and H.K. Seidlitz. 1994. Xenon lighting adjusted to plant requirements, p 229-242.

[11] R. N. Hall, "Electron-Hole Recombination in Germanium," Phys.Rev., 1952, 87, 387.

[12] R. Haynes and W. Shcekley, "The Mobility and Life of Injected Holes and Electrons in Germanium," Phys.Rev., 1951, 81, 835. https://doi.org/10.1063/1.1433906.

[13] W. Shockley and W. T. Read, “Statistics of the Recombinations of Holes and Electrons,” Phys.Rev., 1952, 87, 835.

[14] R. N. Hall, “Recombination processes in semiconductors,” Proc.IEEE., 1960, 106B, 923.

[15] K. Graff and H. Pieper, “The Properties of Iron in Silicon,” J.Electrochem.Soc., 1981, 128, 669.

[16] L. C. Kimerling and J. L. Benton, “Electronically controlled reactions of interstitial iron in silicon,” Physica B., 1983, 116, 297.

[17] G. Zoth and W. Bergholz, “A fast, preparation-free method to detect iron in silicon,” J.Appl.Phys., 1990, 67, 6764.

[18] V. Grivickas and J. Linnros, “Carrier Lifetime-Free Carrier Absorption,” Photoconductivity and Photoluminescence., John Wiley & Sons, Inc., 2012.

[19] A. P. Ramsa, H. Jacobs and F. A. Brand, “Microwave Techniques in Measurement of Lifetime in Germanium,” J.Appl.Phys., 1959, 30, 1054.

[20] H. A. Atwater, “Microwave Measurement of Semiconductor Carrier Lifetimes,” J.Appl.Phys., 1960, 31, 938.

[21] G. K. Wertheim, “Transient Recombination of Excess Carriers in Semiconductors,” Phys.Rev., 1958, 109, 1086.

[22] B. Kramer, S. Gelfman and K. Kalikstein, “Microwave Photoconductivity and Luminescence of ZnS and CdS Phosphors,” Phys.Rev.B., 1972, 6, 556.https://doi.org/10.1155/2007/81350.

[23] Pierre. P. Infelta, Matthus P. DeHaas and John M. Warman, “The study of the transient conductivity of pulse irradiated dielectric liquids on a nanosecond timescale using microwaves,” Rad.Phys.Chem., 1997, 10, 353.

[24] M. P. DeHaas and John M. Warman, “Photon-induced molecular charge separation studied by nanosecond time-resolved microwave conductivity,” Chem.Phys., 1982, 73, 35.

[25] M. Kunst and G. Beck, “The study of charge carrier kinetics in semiconductors by microwave conductivity measurements,” J.Appl.Phys., 1986, 60(10), 3558.

[26] R. A. Sinton and A. Cuevas, “Contactless determination of current–voltage characteristics and minority - carrier lifetimes in semiconductors from quasi - steady - state photoconductance data,” Appl. Phys. Lett., vol. 69, no. 17, pp. 2510–2512, Oct. 1996.

[27] S. Rein, Lifetime spectroscopy: a method of defect characterization in silicon for photovoltaic applications ; with 29 tables. Berlin: Springer, 2005.

[28] L. Huldt, “Optical Method for Determining Carrier Lifetimes in Semiconductors,” Phys. Rev. Lett., vol. 2, no. 1, p. 3, 1959.

[29] N. G. Nilsson, “Determination of carrier lifetime, diffusion length, and surface recombination velocity in semiconductors from photo-excited infrared absorption,” Solid-State Electron., vol. 7, no. 6, pp. 455–463, 1964.

[30] F. Sanii, F. P. Giles, R. J. Schwartz, and J. L. Gray, “Contactless nondestructive measurement of bulk and surface recombination using frequency-modulated free carrier absorption,” Solid-State Electron., vol. 35, no. 3, pp. 311–317, 1992.

[31] F. Sanii, R. J. Schwartz, R. F. Pierret, and W. Au, “The Measurement of Bulk and Surface

Recombination by Means of Modulated Free Carrier Absorption," IEEE J. Photovolt., p. 575.

[32] X. Zhang and B. Li, "Carrier Diffusivity Measurement in Silicon Wafers Using Free Carrier Absorption," Int. J. Thermophys., vol. 34, no. 8–9, pp. 1721–1726, Sep. 2013.

[33] S. Ren, B. Li, and Q. Huang, "Three-dimensional transient model for time-domain free-carrier absorption measurement of excess carriers in silicon wafers," J. Appl. Phys., vol. 114, no. 24, p. 243702, Dec. 2013.

[34] Kevin M.W. Boyd, "Free-Carrier Pump/Probe Spectroscopy," McMaster University, 2018.

[35] D. B. M. Klaassen, "A unified mobility model for device simulation—I. Model equations and concentration dependence," Solid-State Electron., vol. 35, no. 7, pp. 953–959, 1992.

[36] D. K. Schroder, R. N. Thomas, and J. C. Swartz, "Free carrier absorption in silicon," IEEE J. Solid-State Circuits, vol. 13, no. 1, pp. 180–187, 1978.

[37] P. Zheng, F. E. Rougieux, D. Macdonald, and A. Cuevas, "Measurement and Parameterization of Carrier Mobility Sum in Silicon as a Function of Doping, Temperature and Injection Level," IEEE J. Photovolt., vol. 4, no. 2, pp. 560–565, Mar. 2014.

[38] B. K. Ridley, Quantum Processes in Semiconductors. OUP Oxford, 2013.

[39] S. C. Baker-Finch, K. R. McIntosh, D. Yan, K. C. Fong, and T. C. Kho, "Near-infrared free carrier absorption in heavily doped silicon," J. Appl. Phys., vol. 116, no. 6, p. 063106, Aug. 2014.

[40] J.Isenberg and W. Warta, "Free carrier absorption in heavily doped silicon layers," Appl. Phys. Lett., vol. 84, no. 13, pp. 2265–2267, Mar. 2004.

[41] G. N. Koskowich, M. Soma, and R. B. Darling, “Near-infrared free-carrier optical absorption in silicon: effect of first-order phonon-assisted scattering in a nonparabolic conduction band,” Phys. Rev. B, vol. 41, no. 5, p. 2944, 1990.

[42] Li, Sheng S., ed. (2006). Semiconductor Physical Electronics. doi:10.1007/0-387-37766-2. ISBN 978-0-387-28893-2.

[43] Nisoli, Mauro. (2016). Semiconductor Photonics. Societa Editrice Esculapi. ISBN 978-8893850025. OCLC 964380194.

[44] Justin Iveland; Lucio Martinelli; Jacques Peretti; James S. Speck and Claude Weisbuch. "Cause of LED Efficiency Droop Finally Revealed," Physical Review Letters., 2013. Science Daily. Retrieved 23 April 2013.

[45] Hall, R.N, "Germanium rectifier characteristics," *Physical Review*., 1951, **83** (1): 228.

[46] Nelson, Jenny, The Physics of Solar Cells. London: Imperial College Press. p. 116. ISBN 978-1-86094-340-9.

[47] Eades, W.D.; Swanson, R.M. (1985). "Calculation of surface generation and recombination velocities at the Si-SiO2 interface". Journal of Applied Physics. 58 (11): 4267–4276. doi:10.1063/1.335562. ISSN 0021-8979.

[48] J. Linnros, “Carrier lifetime measurements using free carrier absorption transients. I. Principle and injection dependence,” J. Appl. Phys., vol. 84, no. 1, p. 275, 1998.

[49] M. Rosling, H. Bleichner, P. Jonsson, and E. Nordlander, “The ambipolar diffusion coefficient in silicon: Dependence on excess-carrier concentration and temperature,” J. Appl. Phys., vol. 76, no. 5, pp. 2855–2859, Sep. 1994.

[50] K. L. Luke and L. Cheng, “Analysis of the interaction of a laser pulse with a silicon wafer: Determination of bulk lifetime and surface recombination velocity,” J. Appl. Phys., vol. 61, no. 6, pp. 2282–2293, Mar. 1987.

[51] Marcos A. C. de Araújo, Rubens Silva, Emerson de Lima, Daniel P. Pereira, and Paulo C. de Oliveira, “Measurement of Gaussian laser beam radius using the knife-edge techniques: Improvement on data analysis,” Applied Optics., vol. 48, no. 2, pp. 393–396, Jan. 2009.